AN IMPROVED METHOD FOR SWING STATE ESTIMATION IN ROTORCRAFT SLUNG–LOAD APPLICATIONS

Emanuele L. de Angelis[*,1], Fabrizio Giulietti[2]

University of Bologna, Department of Industrial Engineering (DIN), CIRI Aerospace, Forlí, Italy 47121

Abstract

In the present paper a method is proposed to estimate the swing state of a suspended payload carried by a single rotorcraft. Starting from the equations of motion of the coupled slung–load system, defined by two point–masses interconnected by a rigid link, a Kalman Filter is developed to estimate cable swing angle and rate from acceleration measurements available from onboard IMU, without the need for extra sensors. The estimation problem is solved according to a nonlinear approach, thus reducing modeling errors with respect to a linear framework and guaranteeing accuracy also in non–hovering conditions and agile maneuvers. Filter performance is enhanced by accounting for aerodynamic disturbance force, whose knowledge is proven to be fundamental in forward flight or in windy conditions. The approach is validated by numerical simulations through an octarotor platform detailed with blade element characterization of propellers and equipped with an elastic cable. It is shown that the output of the estimation problem can be used as a feedback term to reduce payload oscillations, with benefits on flying qualities and energy demand. For the first time the algorithm is also validated on a small–scale quadrotor through an outdoor experimental campaign, thus demonstrating the effectiveness of the approach in a real application scenario.

1. INTRODUCTION

While envisaging complex air delivery scenarios for unmanned rotorcraft, two approaches are generally considered. The first consists in equipping the vehicle with graspers or a sufficiently large cargo compartment, leading to increased take–off mass and complexity, reduced flight endurance and range, and typically degraded agility (Refs. 1 and 2). The second approach consists in the adoption of cable–suspended configurations, which relatively preserve the performance of the aircraft and the simplicity of systems, but they introduce additional non–actuated degrees of freedom that are inherently related to the oscillatory motion. Also, the payload induces forces and moments that can significantly affect the motion of the lifting vehicle. At the same time, the oscillations may damage the payload or its environment after collision with obstacles (Ref. 3).

The problem of a single rotorcraft carrying a load has been addressed in the literature considering minimal load swing, with a number of works investigating different control approaches (Refs. 4–12). In this respect, the accurate measurement of load position information is an important requirement to achieve anti–sway capabilities, with solutions that are often mutuated from overhead crane applications (Ref. 13). Conventional methods include the use of motion capture systems, where accurate estimation comes at the cost of complex and expensive installations (Refs. 14 and 15). Although optical–based alternatives can be conceived, such as visual detection (Ref. 16), they require extra sensor devices that cause a growth of take–off weight and power consumption or vulnerability to environmental conditions (For example, system efficiency may be degraded by dust, sunlight, and air pollution when used in outdoor applications, Ref. 17).

Methods that are not based on the use of ad hoc camera installations rely on devices that are fixed with respect to the load. It is the case of Real–Time Kinematic (RTK) instrumentations (Ref. 18), whose application would be needed for both the rotorcraft and the load in outdoor scenarios. In Ref. 19 a novel method for measuring the sway angle by using an inclinometer attached to the load is proposed. In Ref. 20 the use of rotary potentiometers is adopted to estimate the orientation of appendages for aerial manipulation tasks, with the possibility to perform swing angle measurements of suspended rigid links. In Ref. 21 a swing angle estimation method is developed without any external sensors except an attached IMU module. First, the authors derive an estimation algorithm of the disturbance force

[*] Corresponding author
[1] Assistant Professor, emanuele.deangelis4@unibo.it
[2] Associate Professor, fabrizio.giulietti@unibo.it

caused by the slung load using a disturbance observer. Since the direction of the tension force is the same as the direction of the wire when it is taut, the swing angle is directly estimated from force components. The limitations of the method are pointed out and discussed, based on the inherent difficulty to discriminate the load–induced forces from propulsive or other disturbance contributions. To this end, the authors suggest a practical alternative where a single load–cell is mounted on the tether. In a recent work by one of the authors of the present paper (Ref. 22), a method is presented to estimate swing angles in multirotor applications, with no need to rely on extra sensors except for the accelerometers already available on board. Sensor readings and dynamic model information are fused by means of a Fading Gaussian Deterministic Filter (FGDF), based on a recursive linear formulation derived in Ref. 23. The approach is validated by numerical simulations and filter performance is measured and optimized in the presence of model uncertainties and measurement errors.

In the present paper the filtering approach described in Ref. 22 is reformulated and improved with the aim to overcome some limitations related to the original setup. First, the point–mass equations of the coupled slung–load system are derived through the Lagrangian approach, based on the assumption of a mass–less and rigid cable. An Extended Kalman Filter (EKF) is proposed to outline the estimation problem, thus reducing modeling errors with respect to the linear framework and guaranteeing accuracy also in non–hovering conditions and agile maneuvers. At the same time it is shown that the proposed approach is strongly affected by the correct modeling of aerodynamic forces on both the airframe and the rotors, which becomes evident in forward flight and in the presence of wind. The state of EKF is thus extended by including the three components of aerodynamic disturbance forces, projected in the inertial frame. To this end, a solution is proposed to reconstruct the overall thrust generated by the rotors, isolate it from other aerodynamic force contributions and avoid the need for the load cell adopted in Ref. 21.

The proposed algorithm is first validated by numerical simulations. Test cases in a non–nominal scenario are described where a battery–powered octarotor is modeled as a rigid body equipped with an elastic cable. System description is detailed in terms of electric propulsion system components and Blade Element characterization of propellers (Refs. 24 and 25). Environmental disturbances and model uncertainties are accounted and state estimation is evaluated during sample maneuvers, showing satisfactory accuracy for both swing state and aerodynamic disturbance characterization. For the first time the algorithm is also validated through an outdoor experimental campaign in windy conditions, which is another contribution of this paper. After deployment of the recursive algorithm to a commercial–off–the–shelf Pixhawk computer, filter performance is analyzed for a small–scale quadcopter equipped with a two–axis potentiometer calibrated for direct measurement of cable swing angles. A comparison is thus provided between measured and estimated states for both the original FGDF of Ref. 22 and the updated EKF algorithm, the latter showing improved accuracy.

As a final contribution, the estimated swing angles and rates are used in a proportional feedback control logic aiming at the stabilization of payload oscillations. Controller structure, that stems from the idea in Ref. 12, is designed as an additive contribution to available control loops specifically developed for rotorcraft guidance and possibly shaped in an optimal control fashion (Ref. 26). As a by–product it is shown that, for the same mission, the activation of payload stabilization controller noticeably reduces the energy required from the battery pack with respect to the case when trajectory–tracking only is performed.

In what follows, reference frames and point–mass system dynamic model are derived in Section 2. EKF recursive equations are detailed in Section 3, where the innovation vector is defined as the difference between model–based and measured vehicle accelerations, projected in the inertial frame. Validation is performed in Section 4, where performance of the filter and advantages of minimal–swing strategies are investigated through numerical test cases. The results of experimental tests are finally reported, where EKF and linear FGDF estimations are compared to direct potentiometer readings. A section of concluding remarks ends this paper.

2. SYSTEM MODELING

Starting from the definition of reference frames, a 3 degrees–of–freedom mathematical model is adopted to describe both the rotorcraft and the load. After formulating the control problem, numerical validation is performed for a multirotor assumed to be a rigid body with center of gravity CG.

2.1. Reference frames

Right–handed orthogonal reference frames are introduced according to the definitions in Ref. 24:

1. an Earth-fixed North-East-Down frame, $\mathcal{F}_E = \{O_E; \boldsymbol{x}_E, \boldsymbol{y}_E, \boldsymbol{z}_E\}$: the origin, O_E, is arbitrarily fixed to a point on the Earth's surface, $\boldsymbol{x}_E$ aims in

the direction of geodetic North, $\boldsymbol{z}_E$ points downward along the Earth ellipsoid normal, and $\boldsymbol{y}_E$ completes a right–handed triad. This frame is assumed to be inertial under the assumption of flat and non–rotating Earth;

2. a Body–fixed frame, $\mathcal{F}_B = \{CG; \boldsymbol{x}_B, \boldsymbol{y}_B, \boldsymbol{z}_B\}$: the longitudinal axis $\boldsymbol{x}_B$ is positive out the nose of the rotorcraft in its selected plane of symmetry, $\boldsymbol{z}_B$ aims in the direction of fuselage/frame belly, and $\boldsymbol{y}_B$ completes a right–handed triad.

3. a rotorcraft structural reference frame, $\mathcal{F}_S = \{O_S; \boldsymbol{x}_S, \boldsymbol{y}_S, \boldsymbol{z}_S\}$, used to locate CG and all vehicle components: axes are parallel to the body–fixed frame axes, such that $\boldsymbol{x}_S = -\boldsymbol{x}_B$, $\boldsymbol{y}_S = \boldsymbol{y}_B$, and $\boldsymbol{z}_S = -\boldsymbol{z}_B$. The origin is located at some arbitrary point within the rotorcraft plane of symmetry. Stations (ST) are measured positive aft along the longitudinal axis. Buttlines (BL) are lateral distances, positive to the right, and waterlines (WL) are measured vertically, positive upward.

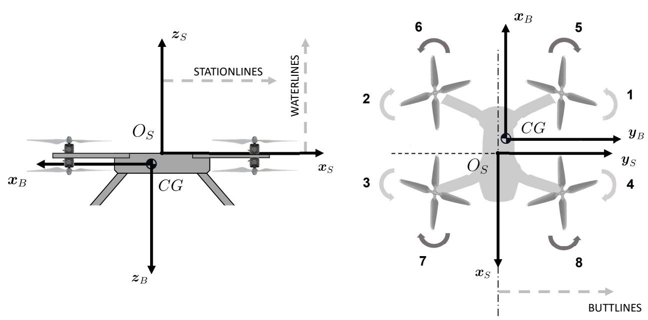

Figure 1: Multirotor body–fixed reference frames.

A sketch of a multirotor including the selected reference frames is reported in Figure 1.

Let $s(\cdot) = \sin(\cdot)$ and $c(\cdot) = \cos(\cdot)$. Vector transformation between $\mathcal{F}_E$ and $\mathcal{F}_B$ is provided by the rotation matrix (Ref. 12):

$$(1) \quad \boldsymbol{T}_{BE}(\boldsymbol{\alpha}) = \begin{bmatrix} c\theta\, c\psi & c\theta\, s\psi & -s\theta \\ s\phi\, s\theta\, c\psi - c\phi\, s\psi & s\phi\, s\theta\, s\psi + c\phi\, c\psi & s\phi\, c\theta \\ c\phi\, s\theta\, c\psi + s\phi\, s\psi & c\phi\, s\theta\, s\psi - s\phi\, c\psi & c\phi\, c\theta \end{bmatrix}$$

obtained by a 3-2-1 Euler rotation sequence where $\boldsymbol{\alpha} = [\phi,\, \theta,\, \psi]^T$ describes the attitude of the rotorcraft in terms of classical 'roll', 'pitch', and 'yaw' angles, respectively. The following notation is adopted: if $\boldsymbol{w}$ is an arbitrary vector, its components are transformed from $\mathcal{F}_E$ to $\mathcal{F}_B$ through $\boldsymbol{w}_B = \boldsymbol{T}_{BE}\, \boldsymbol{w}_E$. In what follows, the subscript E will be dropped for simplicity.

In addition to the reference frames introduced above, a third useful definition is provided for a particular Local–Vertical Local–Horizontal frame, $\mathcal{F}_H = \{CG; \boldsymbol{x}_H, \boldsymbol{y}_H, \boldsymbol{z}_H\}$, with origin in CG. Vector transformation between $\mathcal{F}_B$ and $\mathcal{F}_H$ is provided by rotation matrix $\boldsymbol{T}_{BH} = \boldsymbol{T}_{BE}(\boldsymbol{\alpha}_0)$, where $\boldsymbol{\alpha}_0 = [\phi,\, \theta,\, 0]^T$ is characterized by null elementary rotation about $\boldsymbol{z}_E$. Although the definition of $\mathcal{F}_H$ does not provide additional information to vehicle attitude characterization, which is defined by $\boldsymbol{T}_{BE}$, it will be useful in Section 4 for the outline of a proposed cable–swing controller.

2.2. Equations of motion

Let $\boldsymbol{p} = [p_1,\, p_2,\, p_3]^T$ be the position of multirotor and $\boldsymbol{v} = [v_1,\, v_2,\, v_3]^T$ its velocity with respect to $\mathcal{F}_E$. A suspended load with mass m_l is connected by a cable to the multirotor, as depicted in Fig. 2.

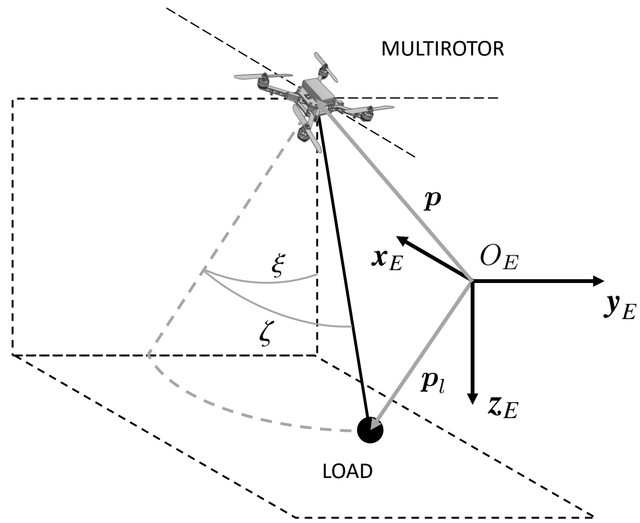

Figure 2: Definition of cable swing angles.

The dynamics of the vehicle as expressed in $\mathcal{F}_E$ is described by the following equations:

$$(2) \quad \dot{\boldsymbol{p}} = \boldsymbol{v}$$

$$(3) \quad m\,\dot{\boldsymbol{v}} = \boldsymbol{f}_g + \boldsymbol{f}_l + \boldsymbol{f}_a + \boldsymbol{f}_c$$

where m is mass of the rotorcraft, $\boldsymbol{f}_g = [0,\, 0,\, m\,g]^T$ is gravity force vector, $\boldsymbol{f}_l$ is the force induced by the load on the rotorcraft through the cable, and $\boldsymbol{f}_a = [f_{a_1},\, f_{a_2},\, f_{a_3}]^T$ is vehicle aerodynamic force, that accounts for the contributions of rotorcraft frame and rotor in–plane forces. The net thrust vector $\boldsymbol{f}_c = [f_{c_1},\, f_{c_2},\, f_{c_3}]^T$, directed along $\boldsymbol{z}_B$ and pointing upwards, represents the only control input to Eq. (3).

The load is assumed to be a point–mass and the cable is connected to the center of gravity of the rotorcraft, such that $\boldsymbol{f}_l$ has no effect on attitude dynamics of the vehicle. For the aim of the present analysis, the cable is modeled as mass–less and rigid with constant length, that are reasonable assumptions if non–aggressive vertical maneuvers are performed and the cable remains in tension. Payload position with respect to the rotorcraft is parametrized by angles $-\pi/2 < \xi < \pi/2$ and $-\pi/2 < \zeta < \pi/2$, respectively obtained from load rotations about $\boldsymbol{x}_H$- and $\boldsymbol{y}_H$-axis. Payload absolute position $\boldsymbol{p}_l = [p_{l1},\, p_{l2},\, p_{l3}]^T$ in $\mathcal{F}_E$ is thus expressed as a function of ξ, ζ, and $\boldsymbol{p}$ as

$$\boldsymbol{p}_l = \boldsymbol{p} + L\,[\sin\zeta, \quad -\sin\xi\,\cos\zeta, \quad \cos\xi\,\cos\zeta]^T \tag{4}$$

where L is nominal length of the cable. Let $\boldsymbol{\lambda} = [\boldsymbol{p}^T,\, \xi,\, \zeta]^T \in \mathbb{R}^5$ be a vector of generalized coordinates. Using Lagrangian method as in Ref. 11, the Lagrangian equation with respect to the generalized coordinate vector $\boldsymbol{\lambda}$ is

$$\frac{d}{dt}\left(\frac{\partial E}{\partial \dot{\boldsymbol{\lambda}}}\right) - \frac{\partial E}{\partial \boldsymbol{\lambda}} = \boldsymbol{\tau} \tag{5}$$

where $E = K - U$ is Lagrangian function and $\boldsymbol{\tau} \in \mathbb{R}^5$ is the vector of generalized forces. In the present framework, K is system kinetic energy, given by

$$K = \frac{1}{2} m\, \dot{\boldsymbol{p}}^T \dot{\boldsymbol{p}} + \frac{1}{2} m_l\, \dot{\boldsymbol{p}}_l^T \dot{\boldsymbol{p}}_l \tag{6}$$

where $\dot{\boldsymbol{p}}_l$ denotes load velocity as obtained from Eq. (4), namely:

$$\dot{\boldsymbol{p}}_l = \dot{\boldsymbol{p}} + L\,[\dot{\zeta}\, c\zeta, \quad -\dot{\xi}\, c\xi\, c\zeta + \dot{\zeta}\, s\xi\, s\zeta, \quad -\dot{\xi}\, s\xi\, c\zeta - \dot{\zeta}\, c\xi\, s\zeta]^T \tag{7}$$

Potential energy U is related to the vertical displacement of the multirotor and the suspended load. It is:

$$U = -m\, g\, p_3 - m_l\, g\, p_{l3} \tag{8}$$

Given the energy contributions in Eqs. (6) and (8) and taking into account the state of the load as described by Eqs. (4) and (7), the Lagrangian equation is manipulated into the system:

$$\dot{\boldsymbol{\lambda}} = \boldsymbol{\mu} \tag{9}$$

$$\boldsymbol{M}(\boldsymbol{\lambda})\, \dot{\boldsymbol{\mu}} + \boldsymbol{C}(\boldsymbol{\lambda}, \boldsymbol{\mu})\, \boldsymbol{\mu} + \boldsymbol{G}(\boldsymbol{\lambda}) = \boldsymbol{\tau} \tag{10}$$

where $\boldsymbol{\mu} = [\boldsymbol{v}^T,\, \dot{\xi},\, \dot{\zeta}]^T \in \mathbb{R}^5$ and

$$\boldsymbol{M}(\boldsymbol{\lambda}) = L\, m_l \begin{bmatrix} M/(L\, m_l) & 0 & 0 & 0 & c\zeta \\ 0 & M/(L\, m_l) & 0 & -c\xi\, c\zeta & s\xi\, s\zeta \\ 0 & 0 & M/(L\, m_l) & -s\xi\, c\zeta & -c\xi\, s\zeta \\ 0 & -c\xi\, c\zeta & -s\xi\, c\zeta & L\, c^2\zeta & 0 \\ c\zeta & s\xi\, s\zeta & -c\xi\, s\zeta & 0 & L \end{bmatrix} \tag{11}$$

$$\boldsymbol{C}(\boldsymbol{\lambda}, \boldsymbol{\mu}) = L\, m_l \begin{bmatrix} 0 & 0 & 0 & 0 & -\dot{\zeta}\, s\zeta \\ 0 & 0 & 0 & \dot{\xi}\, s\xi\, c\zeta + \dot{\zeta}\, c\xi\, s\zeta & \dot{\xi}\, c\xi\, s\zeta + \dot{\zeta}\, s\xi\, c\zeta \\ 0 & 0 & 0 & -\dot{\xi}\, c\xi\, c\zeta - \dot{\zeta}\, s\xi\, s\zeta & \dot{\xi}\, s\xi\, s\zeta - \dot{\zeta}\, c\xi\, c\zeta \\ 0 & 0 & 0 & -L\, \dot{\zeta}\, s\zeta\, c\zeta & -L\, \dot{\xi}\, s\zeta\, c\zeta \\ 0 & 0 & 0 & L\, \dot{\xi}\, s\zeta\, c\zeta & 0 \end{bmatrix} \tag{12}$$

$$\boldsymbol{G}(\boldsymbol{\lambda}) = g\, L\, m_l [0, \quad 0, \quad -M/(L\, m_l), \quad s\xi\, c\zeta, \quad c\xi\, s\zeta]^T \tag{13}$$

provided $M = m + m_l$ is the total mass of the system. The generalized force vector $\boldsymbol{\tau}$ is made of an active control contribution, $\boldsymbol{\tau}_c$, and a dissipative term, $\boldsymbol{\tau}_a$, which mostly accounts for the aerodynamic drag effects. In particular, it is $\boldsymbol{\tau}_c = [\boldsymbol{f}_c^T,\, 0,\, 0]^T$, while $\boldsymbol{\tau}_a = [\boldsymbol{f}_a^T,\, 0,\, 0]^T - \boldsymbol{D}\,\boldsymbol{\mu}$ includes the rotorcraft aerodynamic force $\boldsymbol{f}_a$ and an additional linear damping term incorporating the effects of payload drag at low oscillation speeds, provided $\boldsymbol{D} = \mathrm{diag}(0, 0, 0, d, d)$ and $d > 0$ is a drag coefficient.

Remark 1 The constraints posed on payload displacement prevent singularities determined by the mathematical representation in Eqs. (9)–(13). For example, $\boldsymbol{M}(\boldsymbol{\lambda})$ becomes singular when $\zeta = \pm 90$ deg, which is the case when the cable is directed along the $\boldsymbol{x}_H$–axis. Such a situation violates the assumptions on pendulum model and practically represents a hazardous condition. As a matter of fact, this is unlikely to be encountered in practice. For load transportation applications outside critical and emergency scenarios (i.e. search and rescue, fire fighting), in fact, aggressive maneuvers and/or unusual attitude conditions are not foreseen. In addition, constraints on desired rotorcraft attitude and thrust are typically envisaged while active swing control strategies can mitigate unusual conditions.

3. FILTER RECURSIVE EQUATIONS

Let $\boldsymbol{x} = [\xi,\, \zeta,\, \dot{\xi},\, \dot{\zeta},\, f_{a_1},\, f_{a_2},\, f_{a_3}]^T = [x_1,\, x_2,\, x_3,\, x_4,\, x_5,\, x_6,\, x_7]^T \in \mathbb{R}^7$ be the state vector describing the oscillatory state of the payload and the aerodynamic disturbance affecting the rotorcraft. Define $\boldsymbol{u} = \boldsymbol{f}_c = [u_1,\, u_2,\, u_3]^T \in \mathbb{R}^3$ as the only input vector to the nonlinear system $\dot{\boldsymbol{x}} = \boldsymbol{f}(\boldsymbol{x}, \boldsymbol{u})$, provided

$$\boldsymbol{f}(\boldsymbol{x}, \boldsymbol{u}) = \begin{bmatrix} x_3 \\ x_4 \\ \begin{gathered}[u_2\, \cos(x_1) + x_6\, \cos(x_1) + u_3\, \sin x_1 + x_7\, \sin x_1 \\ + 2\, L\, m\, x_3\, x_4\, \sin x_2]/[L\, m\, \cos(x_2)]\end{gathered} \\ \begin{gathered}-[L\, m\, \cos(x_2)\, \sin(x_2)\, \dot{\xi}^2 + u_1\, \cos(x_2) + x_5\, \cos(x_2) - u_3\, \cos(x_1)\, \sin(x_2) \\ - x_7\, \cos(x_1)\, \sin(x_2) + u_2\, \sin(x_1)\, \sin(x_2) + x_6\, \sin(x_1)\, \sin(x_2)]/(L\, m)\end{gathered} \\ \boldsymbol{0}_{3\times 1} \end{bmatrix} \tag{14}$$

is obtained from Eqs. (9)–(13), with the additional assumptions of constant or slowly–varying disturbance force, namely $\dot{\boldsymbol{f}}_a = \boldsymbol{0}_{3\times 1}$, and null payload drag, $d = 0$. The inertially–fixed acceleration of the rotorcraft is expressed as $\dot{\boldsymbol{v}} = \boldsymbol{h}(\boldsymbol{x}, \boldsymbol{u})$, where

$$\text{(15)} \quad \boldsymbol{h}(\boldsymbol{x},\boldsymbol{u}) = \begin{bmatrix} \begin{aligned} &[u_1\, m + x_5\, m + u_1\, m_l\, \cos^2(x_2) + x_5\, m_l\, \cos^2(x_2) + L\, m\, m_l\, x_4^2\, \sin(x_2) \\ &\quad - u_3\, m_l\, \cos(x_1)\, \cos(x_2)\, \sin(x_2) - x_7\, m_l\, \cos(x_1)\, \cos(x_2)\, \sin(x_2) \\ &\quad + u_2\, m_l\, \cos(x_2)\, \sin(x_1)\, \sin(x_2) + x_6\, m_l\, \cos(x_2)\, \sin(x_1)\, \sin(x_2) \\ &\quad + L\, m\, m_l\, x_3^2\, \cos^2(x_2)\, \sin(x_2)]/(m\, M) \end{aligned} \\ \begin{aligned} &[u_2\, m + x_6\, m + u_2\, m_l + x_6\, m_l - u_2\, m_l\, \cos^2(x_2) - x_6\, m_l\, \cos^2(x_2) \\ &\quad + u_2\, m_l\, \cos^2(x_1)\, \cos^2(x_2) + x_6\, m_l\, \cos^2(x_1)\, \cos^2(x_2) \\ &\quad + u_3\, m_l\, \cos(x_1)\, \cos^2(x_2)\, \sin(x_1) + x_7\, m_l\, \cos(x_1)\, \cos^2(x_2)\, \sin(x_1) \\ &\quad + u_1\, m_l\, \cos(x_2)\, \sin(x_1)\, \sin(x_2) + x_5\, m_l\, \cos(x_2)\, \sin(x_1)\, \sin(x_2) \\ &\quad - L\, m\, m_l\, x_4^2\, \cos(x_2)\, \sin(x_1) - L\, m\, m_l\, x_3^2\, \cos^3(x_2)\, \sin(x_1)]/(m\, M) \end{aligned} \\ \begin{aligned} &[u_3\, m + x_7\, m + u_3\, m_l + x_7\, m_l + g\, m^2 + g\, m\, m_l \\ &\quad - u_3\, m_l\, \cos^2(x_1)\, \cos^2(x_2) - x_7\, m_l\, \cos^2(x_1)\, \cos^2(x_2) \\ &\quad + u_2\, m_l\, \cos(x_1)\, \cos^2(x_2)\, \sin(x_1) + x_6\, m_l\, \cos(x_1)\, \cos^2(x_2)\, \sin(x_1) \\ &\quad - u_1\, m_l\, \cos(x_1)\, \cos(x_2)\, \sin(x_2) - x_5\, m_l\, \cos(x_1)\, \cos(x_2)\, \sin(x_2) \\ &\quad + L\, m\, m_l\, x_4^2\, \cos(x_1)\, \cos(x_2) + L\, m\, m_l\, x_3^2\, \cos(x_1)\, \cos^3(x_2)]/(m\, M) \end{aligned} \end{bmatrix}$$

Let $\hat{\boldsymbol{x}}(t)$ be the estimated state at time t obtained through the EKF predict–update dynamic model:

$$\text{(16)} \quad \dot{\hat{\boldsymbol{x}}}(t) = \boldsymbol{f}\left(\hat{\boldsymbol{x}}(t), \boldsymbol{u}(t)\right) + \boldsymbol{K}(t)\left(\boldsymbol{z}(t) - \boldsymbol{h}\left(\hat{\boldsymbol{x}}(t), \boldsymbol{u}(t)\right)\right)$$

where $\boldsymbol{z}(t) = [a_1,\, a_2,\, a_3]^T \in \mathbb{R}^3$ is the vector of measured acceleration projected in $\mathcal{F}_E$ and $\boldsymbol{z}(t) - \boldsymbol{h}\left(\hat{\boldsymbol{x}}(t), \boldsymbol{u}(t)\right)$ is innovation residual. Model–based prediction is affected by multi–variate process noise $\boldsymbol{w}(t) \sim \mathcal{N}\left(0, \boldsymbol{Q}(t)\right)$ with zero–mean normal distribution $\mathcal{N}$ and covariance $\boldsymbol{Q}(t) \in \mathbb{R}^{7\times 7}$. In the same way, measurement noise $\boldsymbol{\nu}(t)$ characterizes accelerometer readings with covariance matrix $\boldsymbol{R}(t) \in \mathbb{R}^{3\times 3}$. Kalman gain matrix $\boldsymbol{K}(t) \in \mathbb{R}^{7\times 3}$ is derived from

$$\text{(17)} \quad \boldsymbol{K}(t) = \boldsymbol{P}(t)\, \boldsymbol{H}^T(t)\, \boldsymbol{R}^{-1}(t)$$

provided that covariance estimate propagates according to

$$\text{(18)} \quad \begin{aligned} \dot{\boldsymbol{P}}(t) = {} & \boldsymbol{F}(t)\, \boldsymbol{P}(t) + \boldsymbol{P}(t)\, \boldsymbol{F}^T(t) - \boldsymbol{K}(t)\, \boldsymbol{H}(t)\, \boldsymbol{P}(t) \\ & + \boldsymbol{Q}(t) \end{aligned}$$

Finally, the state transition $\boldsymbol{F}(t) \in \mathbb{R}^{7\times 7}$ and observation $\boldsymbol{H}(t) \in \mathbb{R}^{3\times 7}$ matrices are respectively defined as the Jacobians:

$$\text{(19)} \quad \boldsymbol{F}(t) = \left.\frac{\partial \boldsymbol{f}}{\partial \boldsymbol{x}}\right|_{\hat{\boldsymbol{x}}(t), \boldsymbol{u}(t)}, \qquad \boldsymbol{H}(t) = \left.\frac{\partial \boldsymbol{h}}{\partial \boldsymbol{x}}\right|_{\hat{\boldsymbol{x}}(t), \boldsymbol{u}(t)}$$

whose components are listed in the Appendix.

Remark 2 For the aim of the present analysis, input $\boldsymbol{u}(t)$ in Eq. (16) is assumed to be known. As a matter of fact, the exact knowledge of control force is not directly available in practical applications, where detailed models of powerplant subsystems and propellers aerodynamics would be required. In what follows, a sample solution is proposed for multirotor vehicles to address model uncertainty through measurements without the need for ad hoc devices or accurate characterization of propulsion units. Based on the definition in Section 2.2, the control force is expressed as $\boldsymbol{f}_c = -T\, \boldsymbol{z}_B = \boldsymbol{T}_{BE}^T\, [0,\, 0,\, -T]^T$, where T is net thrust generated by rotors along $\boldsymbol{z}_B$. Taking into account Eq. (3), the estimated thrust magnitude $\hat{T}$ can be calculated according to:

$$\text{(20)} \quad \hat{T} = \left\| m\, \boldsymbol{z} - \hat{\boldsymbol{f}}_g - \hat{\boldsymbol{f}}_l - \hat{\boldsymbol{x}}_{5:7} \right\|$$

where $\|\cdot\|$ is Euclidean norm, $\hat{\boldsymbol{f}}_g = [0,\, 0,\, m\, \hat{g}]^T$, $\hat{g}$ is measured gravity acceleration, and $\hat{\boldsymbol{f}}_l = [0,\, 0,\, m_l\, \hat{g}]^T$ is the force induced by the load on the rotorcraft under the assumption that the cable is exactly directed along the local vertical, as it occurs in near–hovering equilibrium condition. Finally, $\hat{\boldsymbol{x}}_{5:7} = [\hat{x}_5,\, \hat{x}_6,\, \hat{x}_7]^T$ is the vector of filter–estimated aerodynamic force, that includes external disturbances and rotor forces over the $\boldsymbol{x}_B - \boldsymbol{y}_B$ plane. Reconstructed input for filtering purposes is thus obtained as $\hat{\boldsymbol{u}} = \hat{\boldsymbol{T}}_{BE}^T\, [0,\, 0,\, -\hat{T}]^T$, provided $\hat{\boldsymbol{T}}_{BE}$ is rotation matrix in Eq. (1), calculated from measured attitude information. Extension of the proposed method to conventional helicopter configurations can be conceived with minimum effort by accounting both tail rotor and main rotor contributions for the estimation of net control force.

4. RESULTS

Filter validation is performed by numerical simulations and an experimental campaign. In the first case, a cargo multirotor is shown to perform sample delivery maneuvers of a relatively large payload with and without the activation of a basic swing–damping controller. In the second case, the approach is addressed for a small–scale quadrotor application, provided the estimated swing state is compared to direct measurements obtained through potentiometer readings.

4.1. Simulation results

4.1.1. Simulation setup

Simulations are performed by using Matlab® environment with a 4th–order Runge–Kutta solver frequency of 500 Hz. A multirotor is modeled as a rigid body while the payload is assumed to be a point mass attached through a linear–elastic cable to a hook point H, distinct from the rotorcraft center of gravity CG. The modeling follows the same approach and nomenclature adopted in Ref. 12 while relevant system parameters are listed in Table 1. The payload is affected by aerodynamic drag, provided $A_l = \pi\, R_l^2$ is frontal area of an equivalent sphere with radius $R_l = 0.5$ m and drag coefficient

$C_{dl} = 0.5$. An octarotor platform is considered, characterized by a set of 4 contra–rotating propellers (see Figure 1). The cross–shaped planar configuration is characterized by $STA_{R_1} = STA_{R_2} = STA_{R_5} = STA_{R_6} = -STA_{R_3} = -STA_{R_4} = -STA_{R_7} = -STA_{R_8} = -0.690$ m, $BL_{R_1} = BL_{R_4} = BL_{R_5} = BL_{R_8} = -BL_{R_2} = -BL_{R_3} = -BL_{R_6} = -BL_{R_7} = 0.690$ m, $WL_{R_1} = WL_{R_2} = WL_{R_3} = WL_{R_4} = -0.024$ m, and $WL_{R_5} = WL_{R_6} = WL_{R_7} = WL_{R_8} = -0.238$ m.

Table 1: Multirotor slung–load system parameters

Parameter	Symbol	Value	Units
Multirotor			
Mass	m	70	kg
Center of gravity position	$STA_{CG} = BL_{CG}$	0	m
	WL_{CG}	-0.15	m
Moments of inertia	J_{11}	10.61	kg m^2
	J_{22}	10.31	kg m^2
	J_{33}	19.74	kg m^2
	J_{12}	0.037	kg m^2
	J_{13}	-0.043	kg m^2
	J_{23}	-0.003	kg m^2
Center of pressure position	$STA_{CP} = BL_{CP}$	0	m
	WL_{CP}	-0.125	m
Frame drag areas	$A_1 = A_2$	0.22	m^2
	A_3	1.03	m^2
Propeller			
Number of blades	n_b	2	
Radius	R	0.5	m
Mean aerodynamic chord	$\bar{c}$	0.086	m
Chord @ $75\% R$	c_{75}	0.103	m
Lift curve slope	a	5.9	rad^{-1}
Pre–cone angle	a_0	0	rad
Root pitch angle	θ_0	0.7854	rad
Total twist	θ_t	-0.6981	rad
Load			
Mass	m_l	100	kg
Reference area	A_l	0.785	m^2
Drag coefficient (sphere)	C_{dl}	0.5	
Cable			
Nominal cable length	L	15	m
Hooke's constant	K	90 950	N/m
Hook point position	$STA_H = BL_H$	0	m
	WL_H	-0.3	m

Rotor forces and moments are calculated by means of Blade Element Momentum Theory. With respect to the thrust and torque contributions only, a simplified model is proposed as in Ref. 12, such that:

$$T_j = k_T\,\Omega_j^2, \quad Q_j = k_Q\,\Omega_j^2 \tag{21}$$

where $k_T = \gamma\,\bar{k}_T$ and $k_Q = \gamma\,\bar{k}_Q$. $\bar{k}_T$ and $\bar{k}_Q$ are positive constants determined experimentally at air density $\bar{\rho}$ while $\gamma = \rho/\bar{\rho}$ is a density scaling parameter. In the present case, upper rotors (1–4) are characterized by $\bar{k}_T\big|_{up} = 2.90 \cdot 10^{-3}$ N/(rad/s)^2 while lower rotors (5–8) present $\bar{k}_T\big|_{down} = 2.20 \cdot 10^{-3}$ N/(rad/s)^2, accounting for reduced efficiency due to wake interaction with upper rotors (Ref. 27). Finally, $\bar{k}_Q = 1.25 \cdot 10^{-4}$ Nm/(rad/s)^2 at the reference density $\bar{\rho} = 1.1229$ kg/m^3. The inflow iterative scheme is solved according to *fzero* Matlab® routine by Dekker with initial condition on the induced speed equal to -10 m/s (Ref. 28). Air parameters are calculated from the International Standard Atmosphere (ISA) model as a function of rotorcraft altitude (Ref. 29).

Guidance, navigation, and control tasks are performed, without loss of generality, through a programmable solution based on Pixhawk standard, which integrates necessary sensors and recursive algorithms for state estimation. In this respect, a cascaded controller based on PX4 architecture and notation (Ref. 30) is assumed to stabilize the multirotor according to different flight modes, from high–level position control to direct attitude regulation (see Figure 3). Provided a detailed analysis of PX4 control functions is out of the scope of the present paper, it is supposed that stabilization of the isolated vehicle is performed according to prescribed flying qualities through a dedicated tuning of control parameters. The dynamics of the single electric propulsion unit made of Electronic Speed Controller (ESC) and brushless motor is modeled by a first–order transfer function with time constant $\tau_{em} = 0.06$ s, accounting for both electric and mechanical non–ideal effects. The transfer function transforms the desired value of angular rate into actual value generated by motor shaft.

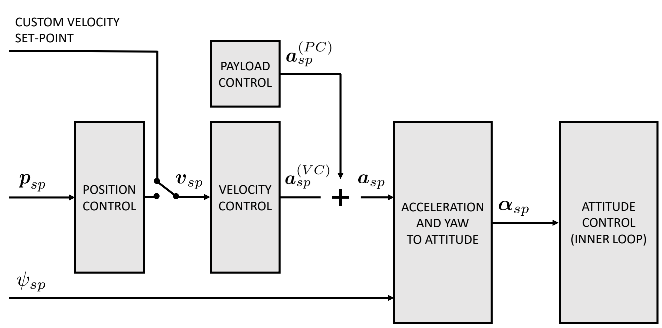

Figure 3: Multirotor and payload control scheme based on PX4 autopilot architecture (Ref. 30).

Onboard computer is located in $STA_{PIX} = BL_{PIX} = 0$ m and $WL_{PIX} = -0.1$ m, with axes aligned with $\mathcal{F}_B$–axes. In order to simulate the effects of sensor noise, zero–mean Gaussian white noise is added to each Euler angle and angular velocity measurement, with standard deviations $\sigma_\alpha = 0.5$ deg and $\sigma_\omega = 0.1$ deg/s, respectively. The body–fixed accelerometer readings are provided by adding white Gaussian noise defined by $\sigma_{acc} = 0.0057$ m/s^2 and a constant bias vector $\boldsymbol{b}_{acc} = [0.015,\,-0.01,\,0.002]^T$ m/s^2 to the simulated values. Estimation error noise is also considered for vehicle position and velocity expressed in $\mathcal{F}_E$, where standard deviations $\sigma_p|_{xy} = 0.074$ m and $\sigma_v|_{xy} = 0.057$

m/s affect motion over the local–horizontal plane, while $\sigma_p|_z = 0.034$ m and $\sigma_v|_z = 0.036$ m/s characterize the vertical channel. Sampling is performed by a frequency of 250 Hz (sample time $\Delta t = 0.004$ s), the same adopted for the generation of control signals and the state–estimation routine.

Filter initial state is set to $\hat{\boldsymbol{x}}_0 = \boldsymbol{0}_{7\times 1}$ and the estimated covariance matrix is initialized with $\boldsymbol{P}_0 = \mathrm{diag}(10^{-6},\, 10^{-6},\, 10^{-6},\, 10^{-6},\, 2,\, 2,\, 10^{-5})$. Let $\boldsymbol{I}_m$ be the unit matrix with dimension m. The assigned noise covariance matrix is $\boldsymbol{R} = 3.6 \cdot 10^{-5} \cdot \boldsymbol{I}_3$ m^2/s^4 and process noise is accounted by $\boldsymbol{Q} = \mathrm{diag}(10^{-7},\, 10^{-7},\, 10^{-7},\, 10^{-7},\, 1,\, 1,\, 10^{-7})$, both matrices assumed to be constant. Uncertainties on relevant filter parameters are also introduced on purpose. In particular, it is assumed that the estimated payload mass is $\hat{m}_l = 0.9 \cdot m_l = 90$ kg, with -10% error.

In order to minimize cable swing angles and rates, an auxiliary payload controller (PC) is proposed to generate a set–point acceleration vector $\boldsymbol{a}_{sp}^{(PC)}$ with components expressed in $\mathcal{F}_E$. Such acceleration is added to the contribution $\boldsymbol{a}_{sp}^{(VC)}$ determined by the velocity controller (VC) in Figure 3. With the aim to 1) generate the auxiliary control action or 2) to compare filter–estimated variables with potentiometer readings during experiments, swing angles and rates are conveniently estimated with respect to the local frame $\mathcal{F}_H$, which is obtained if $\boldsymbol{z}$ and $\boldsymbol{u}$ are projected in $\mathcal{F}_H$ (it is noted that, if ψ is a constant or a slowly–varying attitude parameter, $\mathcal{F}_H$ can be assumed to be an inertial frame). The auxiliary controller, based on a heuristic approach, assumes the form:

$$\text{(22)}\quad \boldsymbol{a}_{sp}^{(PC)} = \boldsymbol{T}_{EH}\left(\begin{bmatrix} k_{D\zeta} & 0 & 0 \\ 0 & k_{D\xi} & 0 \\ 0 & 0 & 0 \end{bmatrix}\begin{bmatrix} \dot{\zeta}_H \\ \dot{\xi}_H \\ 0 \end{bmatrix} + \begin{bmatrix} k_{P\zeta} & 0 & 0 \\ 0 & k_{P\xi} & 0 \\ 0 & 0 & 0 \end{bmatrix}\begin{bmatrix} \zeta_H \\ \xi_H \\ 0 \end{bmatrix}\right)$$

where $\boldsymbol{T}_{EH} = \boldsymbol{T}_{BH}^T \boldsymbol{T}_{BE}^T$ accounts for vector transformation between $\mathcal{F}_H$ and $\mathcal{F}_E$ and is defined by an elementary rotation about $\boldsymbol{z}_H$ with amplitude ψ. Control gains are positive with values $k_{D\xi} = k_{D\zeta} = 2$ m/(rad s) and $k_{P\xi} = k_{P\zeta} = 9$ m/(rad s^2).

4.1.2. Preliminary definitions

Indicators are preliminarily defined with the aim to characterize the performance of simulation cases. The effect of payload active stabilization will be thus investigated and performance indices will assess the validity of the approach for each proposed maneuver. 5 different indicators are introduced:

- Maneuver time, t_m. It is the total time required to conclude the considered maneuver, based on a stop criterion. In the present framework, the simulation is stopped when 2 conditions are met, namely: 1) the positioning error $\varepsilon = \left\|\boldsymbol{p}_{sp} - \boldsymbol{p}\right\|$ falls below 0.1 m and 2) cable oscillation angle $\chi \geq 0$ remains bounded below 1 deg for a prescribed time of 10 s. In the case when the considered maneuver does not require position stabilization, t_m is calculated on the basis of condition 2 only. Cable oscillation angle χ is defined as the angle between the local vertical axis and the direction of the cable. Considering the nomenclature adopted in Ref. 12, χ is obtained from the dot product:

  $$\text{(23)}\quad \chi = \arccos\left(\boldsymbol{z}_H \cdot \hat{\boldsymbol{c}}\right)$$

  where $\hat{\boldsymbol{c}} = \boldsymbol{c}/\left\|\boldsymbol{c}\right\|$ is the unit vector directed from the suspension point to the payload.

- Average swing angle, $\bar{\chi}$. It is calculated through the integral

  $$\text{(24)}\quad \bar{\chi} = \frac{1}{t_m}\int_0^{t_m} \chi(s)\, ds$$

  over maneuver time domain. Although $\bar{\chi}$ correctly describes the overall oscillation behavior on average, the integral quantity $\bar{\chi} \cdot t_m = \int_0^{t_m} \chi(s)\, ds$ is also accounted to provide an indication of how much and how long the cable remains far from the vertical equilibrium condition.

- Average swing rate, $\bar{\nu}$. Let $\nu = \dot{\chi}$ be the swing rate, defined as the time derivative of $\chi(t)$. Then, $\bar{\nu}$ is calculated through the integral

  $$\text{(25)}\quad \bar{\nu} = \sqrt{\frac{1}{t_m}\int_0^{t_m} \nu^2(s)\, ds}$$

  Similarly to the case of $\bar{\chi}$, the integral quantity $\sqrt{\int_0^{t_m} \nu^2(s)\, ds}$ is also determined to provide a better indication of how much and how long the swing rate remains far from the equilibrium null condition.

- Average trajectory–tracking error, $\bar{d}$. It is calculated as the integral

  $$\text{(26)}\quad \bar{d} = \frac{1}{t_m}\int_0^{t_m} d(s)\, ds$$

  of the time–dependent variable $d(t) \geq 0$. In the present case, $d(t)$ describes the accuracy of point–to–point positioning maneuvers in the framework of waypoint navigation. Assume A and

B are consecutive waypoints, respectively identified by position vectors $\boldsymbol{p}_A$ and $\boldsymbol{p}_B$. $d(t)$ represents the distance at time t of the vehicle from the direction defined by vector $\boldsymbol{p}_B - \boldsymbol{p}_A$, calculated over the local–horizontal plane $\boldsymbol{x}_E - \boldsymbol{y}_E$.

- Total propulsive energy, E_{prop}. It is the mechanical energy delivered by electrical motors to propellers, evaluated from the integral

$$E_{prop} = \int_0^{t_m} \sum_{i=1}^{8} P_{sh\,i}(s)\, ds \tag{27}$$

where $P_{sh\,i} = Q_i\,\Omega_i$ is the output shaft power generated by the i–th motor, obtained from required torque Q_i and angular rate Ω_i under the assumption of null friction torque.

4.1.3. Filter validation

Different test cases are analyzed to validate both the estimation and the control strategies.

In the first case ('1') the multirotor starts from a hovering condition at $\boldsymbol{p}(0) = [0,\,0,\,-30]^T$ m with $\xi(0) = \zeta(0) = 20$ deg and $\dot{\xi}(0) = \dot{\zeta}(0) = 0$ deg/s and is required to keep the initial position in the absence of wind ($\boldsymbol{p}_{sp} = \boldsymbol{p}(0)$). Stabilization of multirotor position, initially perturbed by payload non–null conditions, occurs with $\boldsymbol{a}_{sp}^{(PC)} = \mathbf{0}_{3\times 1}$ as in Figure 4, where positioning error $\boldsymbol{e}_p = \boldsymbol{p}_{sp} - \boldsymbol{p}$ components are plotted over time.

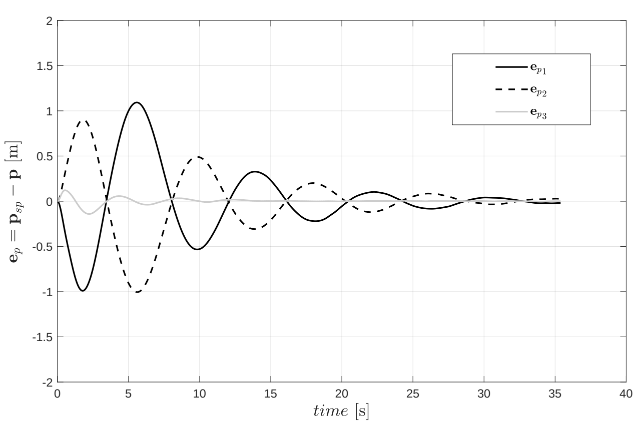

Figure 4: Stabilization of multirotor positioning error (Case 1, no active payload stabilization).

Cable oscillations slowly decay under dissipative effects related to both vehicle speed stabilization and aerodynamic drag affecting the payload, provided maneuver time is $t_m = 35.4$ s. With respect to filter performance, a comparison between the true and the estimated angle and rate is reported in Figure 5, showing convergence of the algorithm.

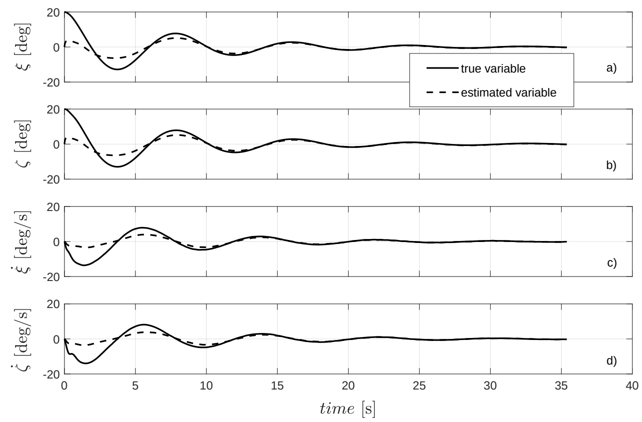

Figure 5: Comparison between the true and the estimated oscillation variables (Case 1, no active payload stabilization).

Assume the auxiliary payload controller is activated with control gains given above. Figure 6 shows the effectiveness of the approach based on the feedback of estimated variables, such that maneuver time is reduced to $t_m = 23.9$ s and oscillation variables are rapidly damped. Cable swing angle χ reaches and remains below 5% of initial value in only 13.5 s, provided the same condition is obtained in about 24.6 s when active payload stabilization does not provide contribution.

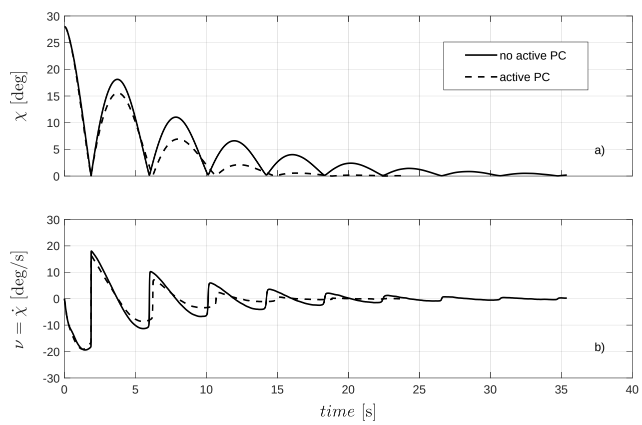

Figure 6: Stabilization of oscillation angle χ and rate ν with and without the activation of payload controller (Case 1).

Table 2: Case 1: summary of performance indicators.

index	no active PC	active PC	error [%]
t_m [s]	35.4	23.9	-32.6
$\bar{\chi}$ [deg]	4.20	4.16	-1
$\bar{\nu}$ [deg/s]	5.53	5.82	+5.2
$\bar{d}$ [m]	0.33	0.63	+90.9
E_{prop} [kJ]	820.7	553.9	-32.5

With respect to other performance indicators, Table 2 summarizes main results and computes percentage errors. Note that the proposed maneuver is representative of a conservative test case, provided the filter is initialized with zero state estimate in the presence of non–zero real state. Such a condition is not encountered in practice and shows in full the phase before filter stabilization (thus affecting closed–loop performance). The activation of PC determines a strong reduction of mechanical energy required to conclude the manueuver, which is determined by the faster decay of oscillation variables. Moreover, if one considers the quantity $\bar{\chi} \cdot t_m$, that is the integral of oscillation angle over maneuver time t_m, a reduction of -33.2% is obtained. Same considerations hold for the integral quantity $\sqrt{\int_0^{t_m} \nu^2(s)\, ds}$, for which a reduction -13.7% is calculated.

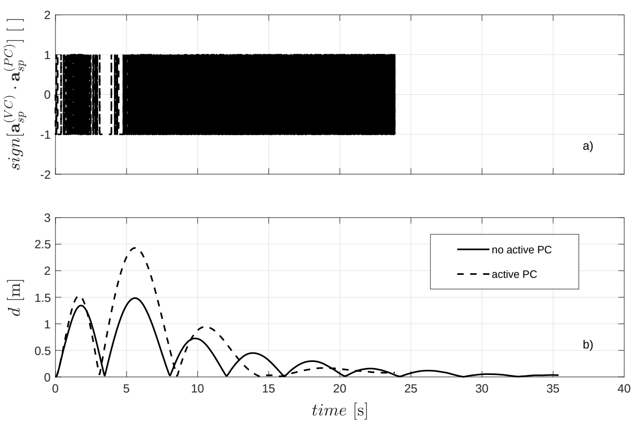

Figure 7: a) analysis of desired acceleration vector contributions; b) stabilization of error distance d with and without the activation of dedicated payload controller (Case 1).

It is noteworthy that improved performance in terms of payload stabilization comes at the cost of increased $\bar{d}$ index ($+90.9\%$). From a physical standpoint, this was to be expected: since the coupled slung–load system is underactuated, both the positioning and the payload control tasks are performed by making the multirotor simultaneously track the desired accelerations $\boldsymbol{a}_{sp}^{(VC)}$ and $\boldsymbol{a}_{sp}^{(PC)}$. The latter contribution is intentionally designed to force the controlled system to exhibit a two–time–scale behavior as in Ref. 11, fast for the oscillation dynamics and slow for the velocity–tracking task. While determining time–scale separation, $\boldsymbol{a}_{sp}^{(PC)}$ perturbs $\boldsymbol{a}_{sp}^{(VC)}$ as in Figure 7, where the sign of the dot product $\boldsymbol{a}_{sp}^{(VC)} \cdot \boldsymbol{a}_{sp}^{(PC)}$ is reported as a function of time, showing partial vector opposition in the very first part of the maneuver (when $t \leq 6$ s). During such phase, d reaches higher values and then rapidly decreases while taking benefit of fast payload stabilization.

In the second case ('2') the multirotor is requested to leave the initial hovering condition with $\xi(0) = \zeta(0) = 0$ deg and $\dot{\xi}(0) = \dot{\zeta}(0) = 0$ deg/s and track the set–point velocity $\boldsymbol{v}_{sp} = [5, 0, 0]^T$ m/s for $t < 30$ s and $\boldsymbol{v}_{sp} = [0, 0, 0]^T$ m/s for $t \geq 30$ s, with components expressed in $\mathcal{F}_E$. A horizontal North wind with constant 1 m/s intensity is assumed to oppose rotorcraft motion.

Table 3: Case 2: summary of performance indicators.

index	no active PC	active PC	error [%]
t_m [s]	66.9	49.0	-26.8
$\bar{\chi}$ [deg]	3.99	2.66	-33.3
$\bar{\nu}$ [deg/s]	5.04	3.86	-23.4
$\bar{d}$ [m]	N/A	N/A	N/A
E_{prop} [kJ]	1 553.1	1 136.5	-26.8

Performance indicators are summarized in Table 3, showing the beneficial effect of $\boldsymbol{a}_{sp}^{(PC)}$. If one considers $\bar{\chi} \cdot t_m$, a reduction of -51.1% is obtained while the integral quantity $\sqrt{\int_0^{t_m} \nu^2(s)\, ds}$ is reduced by -34.4%. Figures 8–10 describe in detail the effect of feedback payload control on multirotor performance. Stabilization of multirotor speed is depicted in Figure 8, where $\boldsymbol{e}_v = \boldsymbol{v}_{sp} - \boldsymbol{v}$ is plotted over time with components in $\mathcal{F}_E$. Comparison between the true and the estimated ζ angle and rate is reported in Figure 9.

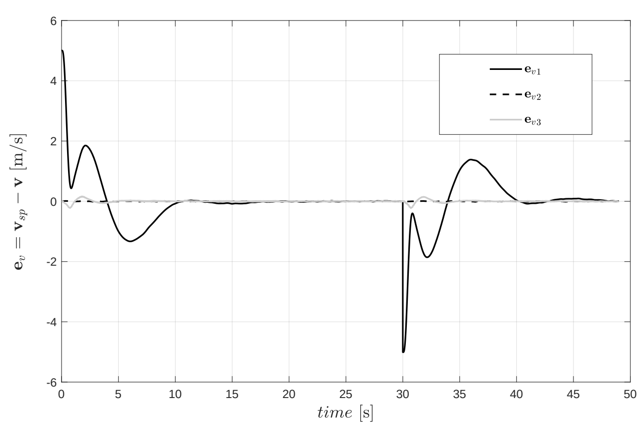

Figure 8: Stabilization of multirotor velocity error (Case 2, active payload stabilization).

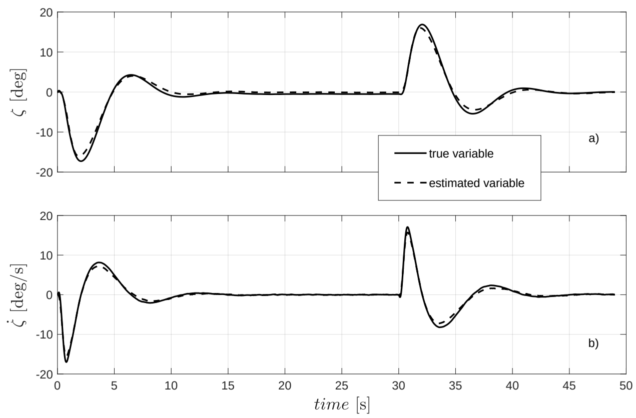

Figure 9: Comparison between the true and the estimated variables ζ and $\dot{\zeta}$ (Case 2, active payload stabilization).

The estimation of disturbance force $\hat{\boldsymbol{f}}_a = \hat{\boldsymbol{x}}_{5:7}$ represents a fundamental task in the present case, where performance of forward flight in the presence of wind is significantly affected by multirotor frame drag and rotor in–plane forces. In Figure 10 estimated disturbance forces are compared to exact variables. It can be noted how EKF is able to track the force components with satisfactory accuracy after the required transients where both multirotor speed and EKF outputs oscillate prior to stabilization. A residual estimation error characterizes the steady–state response of the algorithm (for example, the estimated f_{a2} component sets on a constant value equal to -1.3 N on average, different from the expected zero value). Such a behavior is traceable to the uncertainty in the knowledge of payload mass and the presence of accelerometer bias introduced by $\boldsymbol{b}_{acc}$.

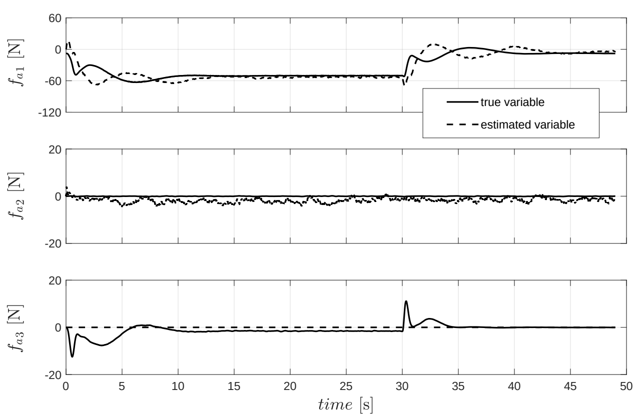

Figure 10: Comparison between the true and the estimated disturbance forces (Case 2, active payload stabilization).

Both non–ideal effects influence algorithm performance in two ways: 1) directly, through EKF equations detailed in Appendix, and 2) indirectly, through input reconstruction as described in Remark 2, where system data and measurement $\boldsymbol{z}$ are used to estimate the generated thrust amplitude. However, it must be pointed out that the considered simulation setup comes under a conservative approach. First, most commercial–off–the–shelf devices, such as Pixhawk platform, already include bias–compensation routines. With respect to the uncertainty on the knowledge of payload mass or cable length, it is recommended to update filter parameters according to the particular flight configuration, provided payload data are preliminary measured or (possibly) online–estimated (Ref. 31). It is the case, for example, when the transportation of goods is performed in large warehouses, where scheduling of system parameters, filter covariance matrix $\boldsymbol{Q}$, and control gains is envisaged according to the cataloged parcel to lift and relocate.

In the third case ('3') the multirotor starts from the same condition of Case 2, it is requested to track a set of prescribed waypoints (see Table 4), and perform a return–to–home maneuver. Each target waypoint is assumed to be reached when its distance from the multirotor decreases below 1.5 m. The first line of Table 4), relative to the first waypoint, coincides with initial multirotor position.

Table 4: Case 3: waypoint list (components expressed in $\mathcal{F}_E$).

$i-$th waypoint	x_i [m]	y_i [m]	z_i [m]
1	0	0	-30
2	10	0	-50
3	20	-10	-50
4	20	10	-50
5	30	0	-50
6	10	0	-50
7	0	0	-30

During the mission gusts are generated to perturb the state of both the multirotor and the payload. The adopted turbulence model, implemented by a dedicate block available from Simulink Aerospace Blockset, adopts the Von Kármán spectral representation to add turbulence by passing band–limited white noise through appropriate forming filters. The approach is based on the mathematical representation in the Military Specification MIL–F–8785C and Military Handbook MIL–HDBK–1797B, respectively cited as Refs. 32 and 33. The following parameters are set:

- specification: MIL-F-8785C;
- model type: continuous Von Kármán (+q +r);
- wind speed at 6 m (used to define the low–altitude wind intensity): 10 m/s;

- wind direction at 6 m (degrees clockwise from North): 90 deg;
- scale length at medium/high altitudes: 533.4 m (default value);
- band–limited noise sample time: 0.002 s;
- MR wingspan: 2.38 m (here intended as the maximum multirotor frontal size);
- load wingspan: 1 m (here intended as the maximum load frontal size).

It is noted that the Simulink–based Von Kármán model is well defined for fixed–wing aircraft, for which non–null speed conditions are expected in flight. This is not the case of multirotors, where the possibility to perform hovering flight makes the wind model not suitable for application. A conservative approach is however adopted where required input speed to the model is calculated as the sum of multirotor actual speed and the maximum desired speed (10 m/s) that the position autopilot of PX4 algorithm is allowed to generate. In addition to the considered turbulence contribution, a horizontal North wind with constant 8 m/s intensity is considered. By taking into account such severe atmospheric conditions, the termination criterion in Section 4.1.2 is conveniently relaxed. In particular, the maneuver is assumed to be concluded when 1) positioning error ε with respect to the last waypoint falls below 0.5 m and 2) cable oscillation angle χ remains bounded below 5 deg for a prescribed time of 10 s.

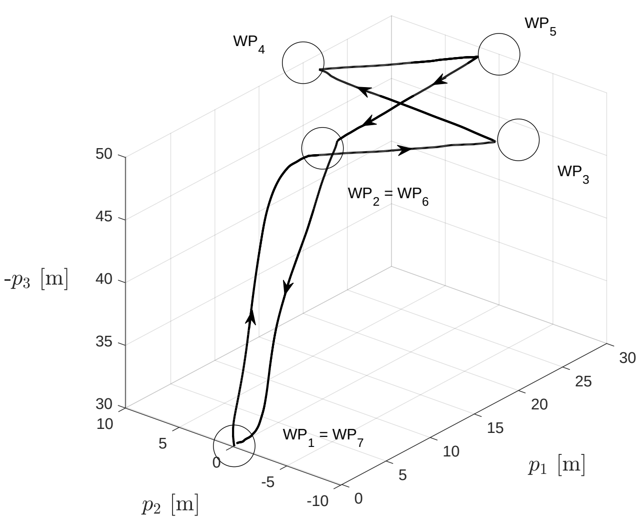

Figure 11: Trajectory followed by the multirotor based on a set of prescribed waypoints (Case 3, no active payload stabilization).

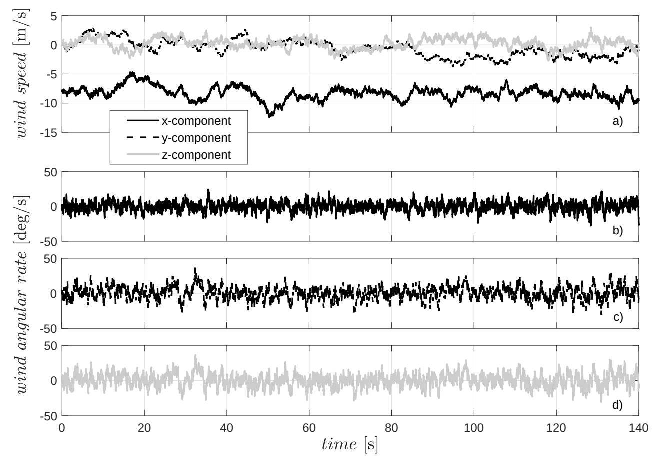

Figure 12: Wind speed and angular rate components projected in $\mathcal{F}_E$ (Case 3, no active payload stabilization).

In Figure 11 the trajectory followed by the multirotor is reported for the case when $\boldsymbol{a}_{sp}^{(PC)} = \boldsymbol{0}_{3\times1}$. Figure 12 depicts wind contributions in terms of linear velocities and angular rates, with components projected in $\mathcal{F}_E$. Obtained performance indicators are reported in the second column of Table 5.

Assume that PC is activated, based on the closed–loop feedback of EKF–estimated variables. The third column of Table 5 summarizes main results and computes percentage errors with respect to the case when no active PC is adopted. As expected, no significant difference characterizes the comparison in terms of both maneuver time and energy, provided that waypoint transition is performed only on the basis of positioning error, with no particular requirement on residual cable swing angle (except for the final waypoint). It is a fact, however, that $\bar{\chi}$ and $\bar{\nu}$ are respectively reduced by 23% and 34.9%, showing improved behavior of swing condition with comparable trajectory–tracking parameter performance, $\bar{d}$ (-0.2%).

Table 5: Case 3: summary of performance indicators.

index	no active PC	active PC (EKF–based)	active PC (FGDF–based)
t_m [s]	140.3	139.8 (-0.4%)	140.3 (+0%)
$\bar{\chi}$ [deg]	2.22	1.71 (-23.0%)	1.77 (-20.3%)
$\bar{\nu}$ [deg/s]	1.86	1.21 (-34.9%)	1.27 (-31.7%)
$\bar{d}$ [m]	6.49	6.48 (-0.2%)	6.52 (+0.5%)
E_{prop} [kJ]	3 242.5	3 230.1 (-0.4%)	3 249.9 (+0.2%)

The proposed approach, based on a nonlinear extended–state estimator, is further validated in Case 3 with respect to the FGDF solution provided in Ref. 22, whose same nomenclature and definitions are adopted. In such a framework, the reduced–order swing state $\boldsymbol{x}^{FGDF} = [\xi, \zeta, \dot{\xi}, \dot{\zeta}]^T \in \mathbb{R}^4$ approximately evolves according to $\dot{\boldsymbol{x}}^{(FGDF)} = \boldsymbol{A}\boldsymbol{x}^{(FGDF)} + \boldsymbol{B}\boldsymbol{u}^{FGDF}$, that is system dynamics obtained from linearization of Eqs. (9)–(13) about the hovering condition. $\boldsymbol{u}^{FGDF} \in$

$\mathbb{R}^2$ accounts for the first two components of $\boldsymbol{u}$, expressed in $\mathcal{F}_H$. By accounting for the same model uncertainties described above, matrices $\boldsymbol{A}$ and $\boldsymbol{B}$ result to be, respectively:

$$(28)\quad \boldsymbol{A} = \begin{bmatrix} 0 & 0 & 1 & 0 \\ 0 & 0 & 0 & 1 \\ -1.4943 & 0 & 0 & 0 \\ 0 & -1.4943 & 0 & 0 \end{bmatrix},$$

$$(29)\quad \boldsymbol{B} = 10^{-4} \cdot \begin{bmatrix} 0 & 0 \\ 0 & 0 \\ 0 & 9.524 \\ -9.524 & 0 \end{bmatrix}$$

In terms of difference equations, the true state vector $\boldsymbol{x}_k^{(FGDF)}$ at time k propagates according to $\boldsymbol{x}_{k+1}^{(FGDF)} = \boldsymbol{\Phi}_k\, \boldsymbol{x}_k^{(FGDF)} + \boldsymbol{\Gamma}_k\, \boldsymbol{u}_k^{(FGDF)}$. Since $\boldsymbol{A}$ is time invariant and non–singular, the state–transition matrix for the estimation algorithm is obtained as $\boldsymbol{\Phi}_k = \boldsymbol{\Phi} = \exp\left(\boldsymbol{A}\,\Delta t\right)$ and implemented by means of Matlab® matrix exponential function $expm(\cdot)$, according to the method in Ref. 34:

$$(30)\quad \boldsymbol{\Phi} = \begin{bmatrix} 1 & 0 & 0.004 & 0 \\ 0 & 1 & 0 & 0.004 \\ -0.006 & 0 & 1 & 0 \\ 0 & -0.006 & 0 & 1 \end{bmatrix}$$

The control–input model is calculated as $\boldsymbol{\Gamma}_k = \boldsymbol{\Gamma} = \boldsymbol{A}^{-1}(\boldsymbol{\Phi} - \boldsymbol{I}_m)\,\boldsymbol{B}$, namely:

$$(31)\quad \boldsymbol{\Gamma} = 10^{-6} \cdot \begin{bmatrix} 0 & 0.008 \\ -0.0088 & 0 \\ 0 & 3.81 \\ -3.81 & 0 \end{bmatrix}$$

The observation $\boldsymbol{z}_k^{(FGDF)} = [\xi_{syn},\, \zeta_{syn}]_k^T \in \mathbb{R}^2$, derived from simple acceleration information as in Ref. 22, approximately tracks the considered dynamic process as in $\boldsymbol{z}_k^{(FGDF)} = \boldsymbol{H}^{(FGDF)}\, \boldsymbol{x}_k^{(FGDF)}$, where

$$(32)\quad \boldsymbol{H}^{(FGDF)} = \begin{bmatrix} 1 & 0 & 0 & 0 \\ 0 & 1 & 0 & 0 \end{bmatrix}$$

is the time–invariant observation matrix. Synthetic angle measurements in $\boldsymbol{z}_k^{(FGDF)}$ are corrupted by noise $\boldsymbol{\nu}_k^{(FGDF)} \in \mathbb{R}^2$ with variance $\boldsymbol{R}^{(FGDF)}$, namely $\boldsymbol{z}_k^{(FGDF)} = \boldsymbol{H}^{(FGDF)}\, \boldsymbol{x}_k^{(FGDF)} + \boldsymbol{\nu}_k^{(FGDF)}$. In the present case, it is $\boldsymbol{R}^{(FGDF)} = 2.465 \cdot 10^{-4} \cdot \boldsymbol{I}_2$ rad^2.

For the sake of brevity, the tuning and scaling procedure described in Ref. 22 to find the globally–optimum FGDF configuration is not reported. Final results are directly provided, where $\beta = \beta_T = 0.998$ represents the best fading factor (in the sense of minimum estimation error) at which the estimated measurement noise covariance matrix $\hat{\boldsymbol{R}}^{(FGDF)}$ satisfies $\hat{\boldsymbol{R}}^{(FGDF)} \approx \boldsymbol{R}^{(FGDF)}$. EKF and FGDF algorithms are switched on in parallel during the maneuver of Case 3 while no active payload stabilization is performed. FGDF is initialized with null state vector and nominal error covariance $(\boldsymbol{E}^{-})_0^{(FGDF)} = 10^{-7} \cdot \boldsymbol{I}_4$.

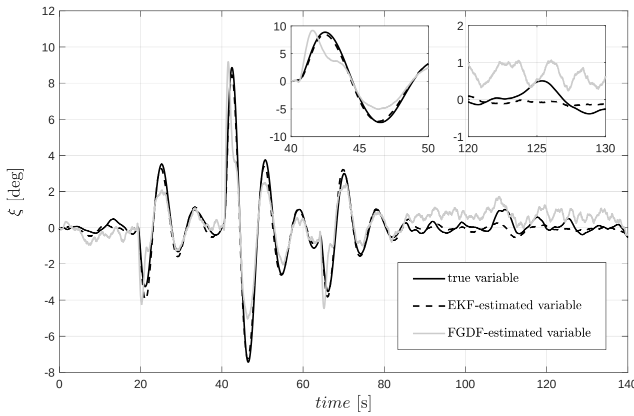

Figure 13: Comparison between the true and the estimated swing angle ξ (Case 3, no active payload stabilization).

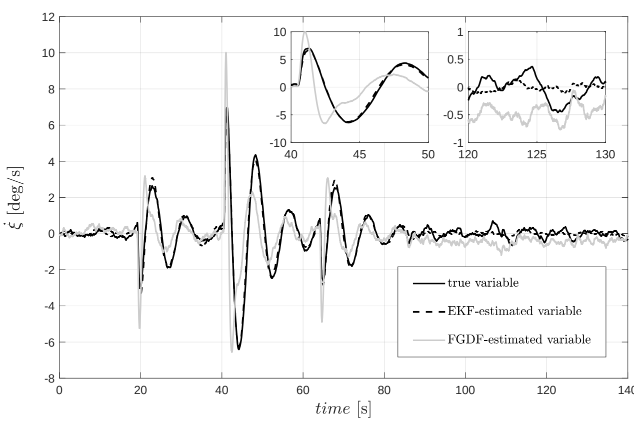

Figure 14: Comparison between the true and the estimated swing rate $\dot{\xi}$ (Case 3, no active payload stabilization).

Figures 13–16 depict the output of the two filters in terms of swing angles and rates. Plot details are also reported to highlight the differences between the results of estimation methods. Improved performance characterizes EKF for all considered variables, especially when high oscillation angles and rates occur (see, for example, what happens during the time interval $40 \leq t \leq 60$ s, when position controller drives the multirotor from WP_3 to WP_4 and excites lateral payload oscillations) or when near–hover flight in the presence of wind is performed. The latter case shows up during time interval $120 \leq t \leq 130$ s, when the multirotor is required to keep the position represented by WP_7 with non–null attitude to counteract the steady wind contribution. During this terminal flight phase, an evident estimation bias characterizes the output of linear algorithm. It is noteworthy that estimation bias of FGDF particularly affects the frontal angle ζ and rate $\dot{\zeta}$, as in Figures 15 and 16. Such a behavior is determined by the presence of a dominant wind contribution from North, that induces disturbance forces on both the vehicle and the suspended load. For the sake of completeness, it is pointed out that estimation error on ζ also characterizes the EKF output (although to a lesser extent). Such drawback comes after neglecting payload drag in both the estimation methods, thus introducing model uncertainty. However, overall EKF performance remains satisfactory and proves to be preferable than that obtained in the linear framework.

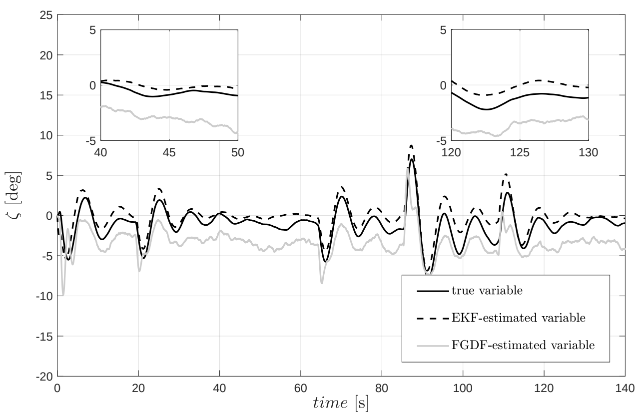

Figure 15: Comparison between the true and the estimated swing angle ζ (Case 3, no active payload stabilization).

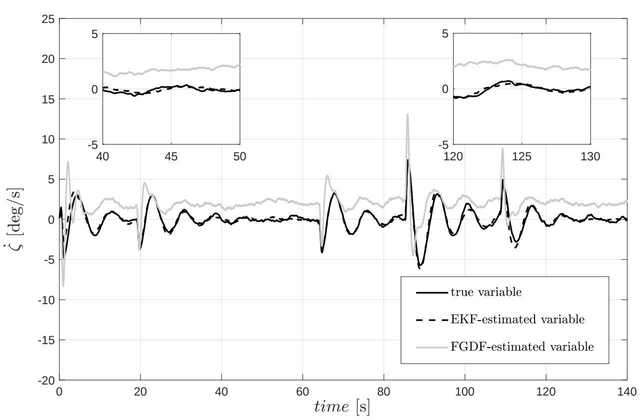

Figure 16: Comparison between the true and the estimated swing rate $\dot{\zeta}$ (Case 3, no active payload stabilization).

In the case when PC is activated based on FGDF information, the mission is performed with indicators listed in the fourth column of Table 5. Despite the macroscopic drawbacks of FGD approach highlighted through Figures 13–16, active payload stabilization still shows to be a successful strategy (although with degraded results in terms of $\bar{\chi}$ and $\bar{\nu}$).

4.2. Experimental results

In order to evaluate the proposed method in a real mission scenario, an experimental campaign is performed by using a Holybro PX4 Development Kit X500 V2 quadcopter with take–off mass $m = 2$ kg and a wheelbase of 0.5 m (see Figure 17.a). The avionics is represented by a Pixhawk® 6X Autopilot Flight Controller with M8N GPS and plug & play SiK Telemetry Radio. The propulsion system is made of 4 BLHeli S ESC 20A compatible with 4S Li–Po Battery, 4 Holybro 2216 KV920 motors, and a planar set of 1045 propellers. The vehicle is equipped with a thin woven rope with nominal length $L = 1.9$ m, suspended by a hook positioned 0.22 m below the multirotor top surface (see Figure 17.b). The hook is fixed to a 2–axis potentiometer system whose signals, sampled at 20 Hz, are acquired by the onboard computer, converted to angles relative to $\mathcal{F}_B$, and corrected by multirotor attitude information to provide direct measurement of oscillation angles ξ and ζ with respect to the local frame $\mathcal{F}_H$. The payload is a ball with radius 0.03 m and mass $m_l = 0.192$ kg.

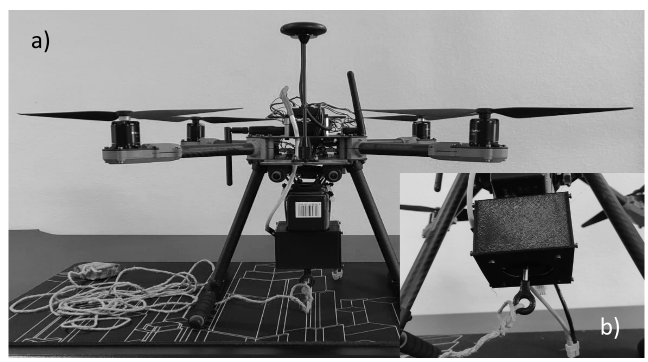

Figure 17: The quadcopter used for experimental campaign (a); the $2-$axis potentiometer system (b).

Flight tests are performed outdoor with environmental temperature of $8°$C and a static pressure of $1\,020$ hPa in the presence of light–unsteady 30 deg NE wind. The multirotor is piloted by imposing desired speed components expressed in $\mathcal{F}_H$ and a desired yaw angle through the remote controller while reaching a maximum altitude of 12 m relative to the ground. The EKF and the FGDF algorithms run simultaneously on the Pixhawk device with a frequency of 100 Hz and no active payload stabilization is performed. With respect to the EKF agorithm, estimated covariance matrix is initialized with $\boldsymbol{P}_0 = \mathrm{diag}(2.2 \cdot 10^{-5},\, 2.2 \cdot 10^{-5},\, 1.3 \cdot 10^{-4},\, 1.3 \cdot 10^{-4},\, 4.3 \cdot 10^{-5},\, 4.3 \cdot 10^{-5},\, 4.3 \cdot 10^{-5})$ and the assigned noise covariance matrix is $\boldsymbol{R} = 3.6 \cdot 10^{-5} \cdot \boldsymbol{I}_3$

m^2/s^4 (the same adopted in Section 4.1). With respect to the FGDF algorithm, it is $\boldsymbol{R}^{(FGDF)} = 2.465 \cdot 10^{-4} \cdot \boldsymbol{I}_2$ rad^2 and $(\boldsymbol{E}^{-})_0^{(FGDF)} = \mathrm{diag}(2.2 \cdot 10^{-5},\, 2.2 \cdot 10^{-5},\, 1.3 \cdot 10^{-4},\, 1.3 \cdot 10^{-4})$ while the state transition matrix and the control–input models are, respectively:

$$(33) \quad \boldsymbol{\Phi} = \begin{bmatrix} 1 & 0 & 0.01 & 0 \\ 0 & 1 & 0 & 0.01 \\ -0.057 & 0 & 1 & 0 \\ 0 & -0.057 & 0 & 1 \end{bmatrix}$$

and

$$(34) \quad \boldsymbol{\Gamma} = 10^{-3} \cdot \begin{bmatrix} 0 & 0.013 \\ -0.013 & 0 \\ 0 & 2.64 \\ -2.64 & 0 \end{bmatrix}$$

Both filters are initialized with null state and the parameters that optimize estimation performance are, respectively, $\beta_T = 0.996$ (FGDF) and $\boldsymbol{Q} = \mathrm{diag}(1, 1, 2, 2, 1, 1, 1) \cdot 10^{-5}$ (EKF), obtained after an intensive experimental campaign.

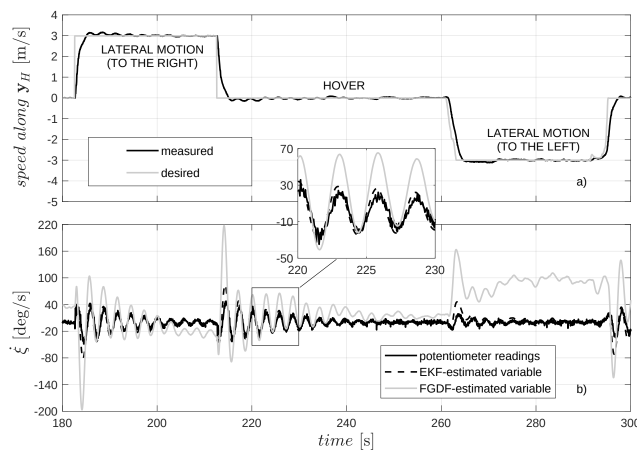

Figure 18: Stabilization of multirotor lateral speed (a); comparison between potentiometer readings and filter–estimated data for $\dot{\xi}$ (b).

In Figure 18.a a sample maneuver is described where the multirotor is required to track a desired lateral speed of ± 3 m/s along $\boldsymbol{y}_H$ with a hovering flight phase in between. A lateral payload oscillation is excited according to Figure 18.b, where angular rate is plotted after numerical derivation and low–pass filtering of potentiometer readings. EKF–based data show very good agreement with direct measurements in all phases, with some over–estimation tendency during transients. FGDF–based data result to be less accurate with a biased behavior that becomes evident when the multirotor is stabilized in the hovering condition and even deteriorates when negative lateral speed is achieved. During the maneuver a disturbance force is observed with values projected over the local horizontal plane equal to -1.5 N and -0.7 N on average, respectively rotated back to $\boldsymbol{x}_E$ and $\boldsymbol{y}_E$. Such results are compatible with the observed direction of wind. The time history of lateral oscillation angle is reported in Figure 19.

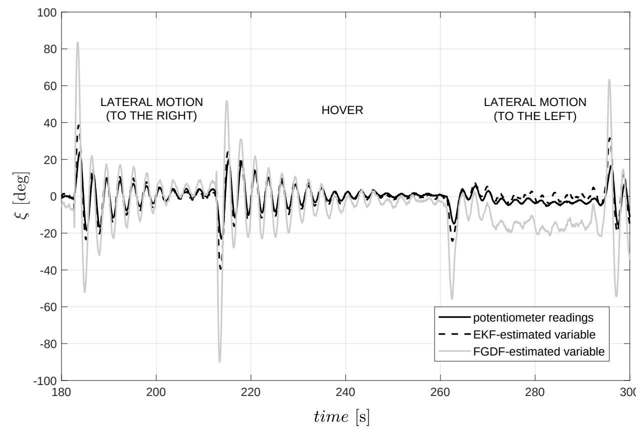

Figure 19: Comparison between potentiometer readings and filter–estimated data for ξ.

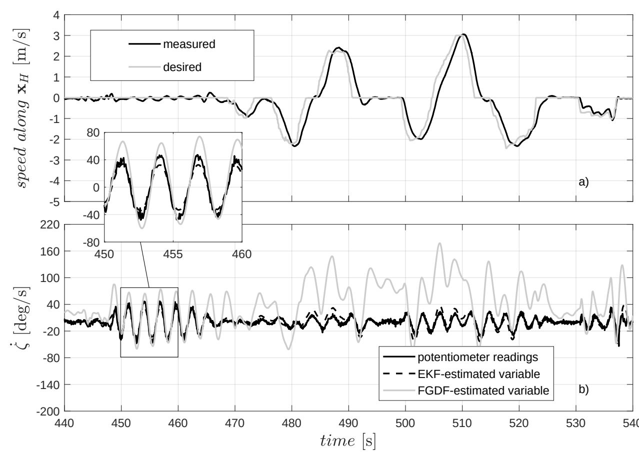

Figure 20: Stabilization of multirotor longitudinal speed (a); comparison between potentiometer readings and filter–estimated data for $\dot{\zeta}$ (b).

In Figures 20 and 21 maneuvers are described to specifically excite headwind payload oscillations. Stabilization of speed along $\boldsymbol{x}_H$ is represented in Figure 20.a, where multirotor starts from a non–nominal hovering condition with residual payload oscillations ($440 \leq t \leq 468$ s) and is then required to track a time–dependent speed profile between -2 and $+3$ m/s ($t > 468$ s). Satisfactory performance characterizes EKF results during the entire maneuver. With regard to FGDF data, acceptable results are obtained during the first phase, despite an evident overestimation of ζ angle near hover. Performance is evidently degraded during the final high–agility maneuver.

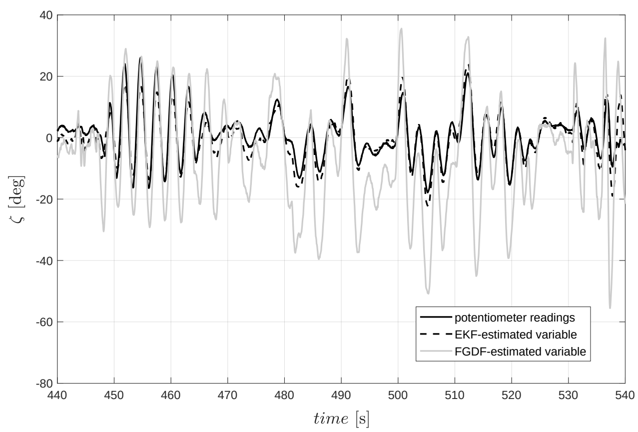

Figure 21: Comparison between potentiometer readings and filter–estimated data for ζ.

5. CONCLUSIONS

In the present paper an estimation algorithm was proposed to characterize the swing state of a suspended load carried by a multirotor. The approach is based an a recursive Kalman formulation where vehicle acceleration measurements are fused with model information in a nonlinear framework. Filter equations are derived for a double point–mass system with a mass–less and rigid cable. Numerical simulations demonstrate the validity of the approach in a realistic simulation scenario, where a highly–nonlinear multirotor vehicle is analyzed in the presence of system uncertainties, external disturbances, and cable elasticity. The nonlinearity of the approach and the possibility to estimate and compensate external disturbances make the filter suitable for inclusion in a closed–loop stabilization framework, where active oscillation damping is shown to determine the reduction of both maneuver time and battery power consumption.

For the first time the proposed algorithm is implemented in a real multirotor platform and an outdoor experimental campaign is performed to address the accuracy of estimation and demonstrate improved performance with respect to that obtainable through a recent work by one of the authors. The approach has the merit of relative simplicity and can be extended for application to any rotorcraft configuration with minimum effort. Results obtained by both numerical and experimental tests prove to be encouraging for future air delivery scenarios where the use of additional sensors, indoor facilities, or ad hoc instrumentation are not contemplated.

6. APPENDIX

In what follows filter recursive equations introduced in Section 3 are detailed. In particular, the non–null components of state transition matrix $\boldsymbol{F}(t)$ and observation matrix $\boldsymbol{H}(t)$ are listed, according to Eqs. (14), (15), and the definitions in Eq. (19):

(35) $F_{13} = F_{24} = 1$

(36) $$F_{31} = (u_3\,\cos x_1 + x_7\,\cos x_1 - u_2\,\sin x_1 \\ - x_6\,\sin x_1)/(L\,m\,\cos x_2)$$

(37) $$F_{32} = 2\,x_3\,x_4 + [\sin x_2\,(u_2\,\cos x_1 + x_6\,\cos x_1 \\ + u_3\,\sin x_1 + x_7\,\sin x_1 \\ + 2\,L\,m\,x_3\,x_4\,\sin x_2)]/(L\,m\,\cos^2 x_2)$$

(38) $F_{33} = 2\,x_4\,\tan x_2$

(39) $F_{34} = 2\,x_3\,\tan x_2$

(40) $F_{36} = \cos x_1/(L\,m\,\cos x_2)$

(41) $F_{37} = \sin x_1/(L\,m\,\cos x_2)$

(42) $$F_{41} = -\sin x_2[(u_2 + x_6)\cos x_1 \\ + (u_3 + x_7)\sin x_1]/(L\,m)$$

(43) $$F_{42} = (u_1\,\sin x_2 + x_5\,\sin x_2 + L\,m\,x_3^2 \\ + u_3\,\cos x_1\,\cos x_2 + x_7\,\cos x_1\,\cos x_2 \\ - u_2\,\cos x_2\,\sin x_1 - x_6\,\cos x_2\,\sin x_1 \\ - 2\,L\,m\,x_3^2\,\cos^2 x_2)/(L\,m)$$

(44) $F_{43} = -x_3\,\sin(2\,x_2)$

(45) $F_{45} = -\cos x_2/(L\,m)$

(46) $F_{46} = -\sin x_1\,\sin x_2/(L\,m)$

(47) $F_{47} = \cos x_1\,\sin x_2/(L\,m)$

(48) $$H_{11} = m_l\,\sin(2\,x_2)[(u_2 + x_6)\cos x_1 \\ + (u_3 + x_7)\sin x_1]/(2\,m\,M)$$

(49) $$H_{12} = -m_l\,[u_1\,\sin(2\,x_2) + x_5\,\sin(2\,x_2) - u_3\,\cos x_1 - x_7\,\cos x_1 + u_2\,\sin x_1 + x_6\,\sin x_1 + 2\,u_3\,\cos x_1\,\cos^2 x_2 + 2\,x_7\,\cos x_1\,\cos^2 x_2 - 2\,u_2\,\cos^2 x_2\,\sin x_1 - 2\,x_6\,\cos^2 x_2\,\sin x_1 - 3\,L\,m\,x_3^2\,\cos^3 x_2 + 2\,L\,m\,x_3^2\,\cos x_2 - L\,m\,x_4^2\,\cos x_2]/(m\,M)$$

(50) $$H_{13} = 2\,L\,m_l\,x_3\,(\sin x_2 - \sin^3 x_2)/M$$

(51) $$H_{14} = 2\,L\,m_l\,x_4\,\sin x_2/M$$

(52) $$H_{15} = (m + m_l\,\cos^2 x_2)/(m\,M)$$

(53) $$H_{16} = m_l\,\cos x_2\,\sin x_1\,\sin x_2/(m\,M)$$

(54) $$H_{17} = -m_l\,\cos x_1\,\cos x_2\,\sin x_2/(m\,M)$$

(55) $$H_{21} = -m_l\,\cos x_2\,(u_3\,\cos x_2 + x_7\,\cos x_2 - u_1\,\cos x_1\,\sin x_2 - x_5\,\cos x_1\,\sin x_2 - 2\,u_3\,\cos^2 x_1\,\cos x_2 - 2\,x_7\,\cos^2 x_1\,\cos x_2 + 2\,u_2\,\cos x_1\,\cos x_2\,\sin x_1 + 2\,x_6\,\cos x_1\,\cos x_2\,\sin x_1 + L\,m\,x_4^2\,\cos x_1 + L\,m\,x_3^2\,\cos x_1\,\cos^2 x_2)/(m\,M)$$

(56) $$H_{22} = -m_l\,[u_1\,\sin x_1 - x_6\,\sin(2\,x_2) - u_2\,\sin(2\,x_2) + x_5\,\sin x_1 - 2\,u_1\,\cos^2 x_2\,\sin x_1 - 2\,x_5\,\cos^2 x_2\,\sin x_1 + 2\,u_2\,\cos^2 x_1\,\cos x_2\,\sin x_2 + 2\,x_6\,\cos^2 x_1\,\cos x_2\,\sin x_2 + 2\,u_3\,\cos x_1\,\cos x_2\,\sin x_1\,\sin x_2 + 2\,x_7\,\cos x_1\,\cos x_2\,\sin x_1\,\sin x_2 - L\,m\,x_4^2\,\sin x_1\,\sin x_2 + 3\,L\,m\,x_3^2\,\sin x_1\,\sin x_2 \cdot (\sin^2 x_2 - 1)]/(m\,M)$$

(57) $$H_{23} = -2\,L\,m_l\,x_3\,\cos^3 x_2\,\sin x_1/M$$

(58) $$H_{24} = -2\,L\,m_l\,x_4\,\cos x_2\,\sin x_1/M$$

(59) $$H_{25} = m_l\,\cos x_2\,\sin x_1\,\sin x_2/(m\,M)$$

(60) $$H_{26} = (m + m_l - m_l\,\cos^2 x_2 + m_l\,\cos^2 x_1\,\cos^2 x_2)/(m\,M)$$

(61) $$H_{27} = (m_l\,\cos x_1\,\cos^2 x_2\,\sin x_1)/(m\,M)$$

(62) $$H_{31} = [m_l\,\cos x_2\,(u_1\,\sin x_1\,\sin x_2 - x_6\,\cos x_2 - u_2\,\cos x_2 + x_5\,\sin x_1\,\sin x_2 + 2\,u_2\,\cos^2 x_1\,\cos x_2 + 2\,x_6\,\cos^2 x_1\,\cos x_2 + 2\,u_3\,\cos x_1\,\cos x_2\,\sin x_1 + 2\,x_7\,\cos x_1\,\cos x_2\,\sin x_1 - L\,m\,x_4^2\,\sin x_1 - L\,m\,x_3^2\,\cos^2 x_2\,\sin x_1)]/(m\,M)$$

(63) $$H_{32} = -[m_l\,\cos x_1\,(2\,u_1\,\cos^2 x_2 - x_5 - u_1 + 2\,x_5\,\cos^2 x_2 + L\,m\,x_4^2\,\sin x_2 - 2\,u_3\,\cos x_1\,\cos x_2\,\sin x_2 - 2\,x_7\,\cos x_1\,\cos x_2\,\sin x_2 + 2\,u_2\,\cos x_2\,\sin x_1\,\sin x_2 + 2\,x_6\,\cos x_2\,\sin x_1\,\sin x_2 + 3\,L\,m\,x_3^2\,\cos^2 x_2\,\sin x_2)]/(m\,M)$$

(64) $$H_{33} = 2\,L\,m_l\,x_3\,\cos x_1\,\cos^3 x_2/M$$

(65) $$H_{34} = 2\,L\,m_l\,x_4\,\cos x_1\,\cos x_2/M$$

(66) $$H_{35} = -m_l\,\cos x_1\,\cos x_2\,\sin x_2/(m\,M)$$

(67) $$H_{36} = m_l\,\cos x_1\,\cos^2 x_2\,\sin x_1/(m\,M)$$

(68) $$H_{37} = (M - m_l\,\cos^2 x_1\,\cos^2 x_2)/(m\,M)$$

7. ACKNOWLEDGMENTS

This study was carried out within the MOST - Sustainable Mobility National Research Center and received funding from the European Union Next-GenerationEU (PIANO NAZIONALE DI RIPRESA E RESILIENZA (PNRR) - MISSIONE 4 COMPONENTE 2, INVESTIMENTO 1.4 - D.D. 1033 17/06/2022, CN00000023). This manuscript reflects only the authors' views and opinions, neither the European Union nor the European Commission can be considered responsible for them.

The authors wish to express their sincerest gratitude to Zephyr S.r.l. for the effective cooperation that allowed the performance of the experimental campaign.

References

[1] P.E.I. Pounds, D.R. Bersak, A.M. Dollar, "Grasping From the Air: Hovering Capture and Load Stability", in: Proc. of IEEE International Conference on Robotics and Automation, 2011, 2491–2498, https://doi.org/10.1109/ICRA.2011.5980314

[2] H. Chen, F. Quan, L. Fang, S. Zhang, "Aerial Grasping with a Lightweight Manipulator Based on Multi–Objective Optimization and Visual Compensation", *Sensors* 19 (2019) 4253, https://doi.org/10.3390/s19194253

[3] X. Li, J. Zhang, J. Han, "Trajectory planning of load transportation with multi–quadrotors based on reinforcement learning algorithm", *Aerosp Sci Technol* 116 (2021) 106887, https://doi.org/10.1016/j.ast.2021.106887

[4] P. Pounds, D. Bersak, A. Dollar, "Stability of small–scale UAV helicopters and quadrotors with added payload mass under PID control", *Auton Robot* 33 (2012) 129–142, https://doi.org/10.1007/s10514-012-9280-5

[5] I. Palunko, R. Fierro, P. Cruz, "Trajectory generation for swing–free maneuvers of a quadrotor with suspended payload: A dynamic programming approach", in: Proc. of 2012 IEEE International Conference on Robotics and Automation, 2012, 2691–2697, https://doi.org/10.1109/ICRA.2012.6225213

[6] S. Dai, T. Lee, D.S. Bernstein, "Adaptive Control of a Quadrotor UAV Transporting a Cable–Suspended load with Unknown Mass", in: Proc. of the 53rd Conference on Decision and Control (CDC), 2014, 6149–6154, https://doi.org/10.1109/CDC.2014.7040352

[7] K. Sreenath, T. Lee, V. Kumar, "Geometric control and differential flatness of a quadrotor UAV with a cable–suspended load", in: Proc. of the 52nd IEEE Conference on Decision and Control (CDC), 2013, 2269–2274, https://doi.org/10.1109/CDC.2013.6760219

[8] M.M. Nicotra, E. Garone, R. Naldi, L. Marconi, "Nested saturation control of an UAV carrying a suspended load, in: Proc. of 2014 American Control Conference", 2014, 3585–3590, https://doi.org/10.1109/ACC.2014.6859222

[9] I.H.B. Pizetta, A.S. Brandão, M. Sarcinelli–Filho, "Modelling and control of a PVTOL quadrotor carrying a suspended load", in: Proc. of 2015 International Conference on Unmanned Aircraft Systems (ICUAS), 2015, 444–450, https://doi.org/10.1109/ICUAS.2015.7152321

[10] J. Potter, W. Singhose, M. Costelloy, "Reducing swing of model helicopter sling load using input shaping", in: Proc. of the 9th IEEE International Conference on Control and Automation (ICCA), 2011, 348–353, https://doi.org/10.1109/ICCA.2011.6138048

[11] E.L. de Angelis, F. Giulietti, G. Pipeleers, "Two–time–scale control of a multirotor aircraft for suspended load transportation", *Aerosp Sci Technol* 84 (2019) 193–203, https://doi.org/10.1016/j.ast.2018.10.012

[12] E.L. de Angelis, F. Giulietti, "Stability and control issues of multirotor suspended load transportation: An analytical closed–form approach", *Aerosp Sci Technol* 135 (2023) 108201, https://doi.org/10.1016/j.ast.2023.108201

[13] T. Wang, J. Zhou, Z. Wu, R. Liu, J. Zhang, Y. Liang, "A Time–Varying PD Sliding Mode Control Method for the Container Crane Based on a Radial–Spring Damper", *Electronics* 11 (2022) 3543, https://doi.org/10.3390/electronics11213543

[14] J.P. How, B. Behihke, A. Frank, D. Dale, J. Vian, "Realtime indoor autonomous vehicle test environment", *IEEE Control Syst* 28(2) (2008) 51–64, https://doi.org/10.1109/MCS.2007.914691

[15] S. Lupashin, M. Hehn, M.W. Mueller, A.P. Schoellig, M. Sherback, R. D'Andrea, "A platform for aerial robotics research and demonstration: the flying machine arena", *Mechatronics* 24(1) (2014) 41–54, https://doi.org/10.1016/j.mechatronics.2013.11.006

[16] M. Zürn, K. Morton, A. Heckmann, A. McFadyen, S. Notter, F. Gonzalez, "MPC controlled multirotor with suspended slung load: system architecture and visual load detection", in: Proc. of IEEE Aerospace Conference, 2016, 1–11, https://doi.org/10.1109/AERO.2016.7500543

[17] M. Ebrahimi, M. Ghayour, S.M. Madani, A. Khoobroo, "Swing angle estimation for anti–sway overhead crane control using load cell", *Int J Control Autom Syst* 9 (2011) 301–309, https://doi.org/10.1007/s12555-011-0212-5

[18] Y. Feng, J. Wang, "GPS RTK Performance Characteristics and Analysis", *J Glob Position Syst* 7(1) (2008), https://doi.org/10.5081/jgps.7.1.1

[19] Y.S. Kim, K.S. Hong, S.K. Sul, “Anti–Sway Control of Container Cranes: Inclinometer, Observer, and State Feedback”, *Int J Control Autom Syst* 2(4) (2004) 435–449, https://doi.org/10.1.1.454.9911

[20] H. Paul, K. Ono, R. Ladig, K. Shimonomura, “A Multirotor Platform Employing a Three–Axis Vertical Articulated Robotic Arm for Aerial Manipulation Tasks”, in: Proc. of IEEE/ASME International Conference on Advanced Intelligent Mechatronics (AIM), 2018, 478–485, https://doi.org/10.1109/AIM.2018.8452699

[21] S.J. Lee, H.J. Kim, “Autonomous Swing–Angle Estimation for Stable Slung–Load Flight of Multi–Rotor UAVs”, in: Proc. of IEEE International Conference on Robotics and Automation (ICRA), 2017, 4576–4581, https://doi.org/10.1109/ICRA.2017.7989532

[22] E.L. de Angelis, “Swing angle estimation for multicopter slung load applications”, *Aerosp Sci Technol* 89 (2019) 264–274, https://doi.org/10.1016/j.ast.2019.04.014

[23] E.L. de Angelis, G. Ferrarese, F. Giulietti, D. Modenini, P. Tortora, “Terminal height estimation using a Fading Gaussian Deterministic filter”, *Aerosp Sci Technol* 55 (2016) 366–376, https://doi.org/10.1016/j.ast.2016.06.013

[24] P.D. Talbot, B.E. Tinling, W.A. Decker, R.T.N. Chen, “A mathematical model of a single main rotor helicopter for piloted simulation”, NASA Technical Memorandum 84281, 1982, 1–52.

[25] J.G. Leishman, *Principles of Helicopter Aerodynamics*, 2nd Edition, Cambridge University Press, New York, 2006, Chs. 2 and 5.

[26] E.L. de Angelis, F. Giulietti, G. Pipeleers, G. Rossetti, R. Van Parys, “Optimal autonomous multirotor motion planning in an obstructed environment”, *Aerosp Sci Technol* 87 (2019) 379–388, https://doi.org/10.1016/j.ast.2019.03.017

[27] H.W. Kim, R.E. Brown, “A Comparison of Coaxial and Conventional Rotor Performance”, *J Am Helicopter Soc* 55 (2010) 012004, 1–20, https://doi.org/10.4050/JAHS.55.012004

[28] G.E. Forsythe, M.A. Malcolm, C.B. Moler, *Computer Methods for Mathematical Computations*, Prentice–Hall, 1976.

[29] U.S. Government Printing Office, “U.S. Standard Atmosphere”, NOAA-S/T 76-1562 (1976) 1–241.

[30] PX4 Development Team and Community, PX4 Autopilot User Guide (main), <https://docs.px4.io/main/en/> (accessed 11/23/2021).

[31] D. Ho, J. Linder, G. Hendeby, M. Enqvist, “Vertical modeling of a quadcopter for mass estimation and diagnosis purposes”, in: Proc. of 2017 Workshop on Research, Education and Development of Unmanned Aerial Systems (RED–UAS), 2017, 192–197, https://doi.org/10.1109/RED-UAS.2017.8101665

[32] U.S. Department of Defense, “Flying Qualities of Piloted Airplanes”, U.S. Military Specification MIL-F-8785C (1980) 1–95.

[33] U.S. Department of Defense, “Flying Qualities of Piloted Aircraft”, U.S. Military Handbook MIL-HDBK-1797B (2012) 1–849.

[34] N.J. Higham, “The Scaling and Squaring Method for the Matrix Exponential Revisited”, *SIAM J Matrix Anal Appl* 26(4) (2005) 1179–1193, https://doi.org/10.1137/04061101X